# Modeling and Stiffness-Based Continuous Torque Control of Lightweight Quasi-Direct-Drive Knee Exoskeletons for Versatile Walking Assistance

Tzu-Hao Huang<sup>®</sup>, Sainan Zhang<sup>®</sup>, Shuangyue Yu<sup>®</sup>, Mhairi K. MacLean, Junxi Zhu<sup>®</sup>, Antonio Di Lallo<sup>®</sup>, Chunhai Jiao, Thomas C. Bulea<sup>®</sup>, *Member, IEEE*, Minghui Zheng<sup>®</sup>, *Member, IEEE*, and Hao Su<sup>®</sup>, *Member, IEEE* 

Abstract—State-of-the-art exoskeletons are typically limited by the low control bandwidth and small-range stiffness of actuators, which are based on high gear ratios and elastic components (e.g., series elastic actuators). Furthermore, most exoskeletons are based on discrete gait phase detection and/or discrete stiffness control, resulting in discontinuous torque profiles. To fill these two gaps, we developed a portable, lightweight knee exoskeleton using quasi-direct-drive (QDD) actuation that provides 14 N·m torque (36.8% biological joint moment for overground walking). This article presents 1) stiffness modeling of torque-controlled QDD exoskeletons and 2) stiffness-based continuous torque controller that estimates knee joint moment in real-time. Experimental tests found that the exoskeleton had a high bandwidth of stiffness control (16 Hz under 100 N·m/rad) and high torque tracking accuracy with 0.34 N·m root mean square error (6.22%) across 0-350 N·m/rad largerange stiffness. The continuous controller was able to estimate knee moments accurately and smoothly for three walking speeds and their transitions. Experimental results with eight able-bodied subjects demonstrated that our exoskeleton was able to reduce the muscle activities of all eight measured knee and ankle muscles by

Manuscript received July 13, 2021; revised December 21, 2021 and April 13, 2022; accepted April 17, 2022. Date of current version June 7, 2022. This work is in part supported by the National Science Foundation CAREER Award under Grant CMMI 1944655, in part by NIH under Grant R01EB029765, in part by under Grant NIDILRR 90DPGE0011, National Science Foundation Future of Work under Grant 2026622. T.C. Bulea was supported by the intramural research program of the NIH Clinical Center. Any opinions, findings, and conclusions, or recommendations expressed in this material are those of the author (s) and do not necessarily reflect the views of the funding organizations. This paper was recommended for publication by Associate Editor J. C. Moreno and Editor M. Yim upon evaluation of the reviewers' comments. (*Tzu-Hao Huang and Sainan Zhang contributed equally to this work.*) (*Corresponding author: Hao Su.*)

Tzu-Hao Huang, Sainan Zhang, Shuangyue Yu, Junxi Zhu, Antonio Di Lallo, Chunhai Jiao, and Hao Su are with the Laboratory of Biomechatronics and Intelligent Robotics, Department of Mechanical and Aerospace Engineering, North Carolina State University, Raleigh, NC 27695 USA (e-mail: d95522013@gmail.com; szhang007@citymail.cuny.edu; yushuangyue0221@gmail.com; jzhu35@ncsu.edu; antoniodilallo.89@hotmail.it; cjiao000@citymail.cuny.edu; hsu4@ncsu.edu).

Mhairi K. MacLean is with the Laboratory of Biomechatronics and Intelligent Robotics, 57522 Enschede, The Netherlands, and also with the Department of Mechanical Engineering, University of Twente, 57522 Enschede, The Netherlands (e-mail: mmaclean@ccny.cuny.edu).

Thomas C. Bulea is with the Functional and Applied Biomechanics Section, Rehabilitation Medicine Department, Clinical Center, National Institutes of Health, Bethesda, MD 20892 USA (e-mail: buleatc@cc.nih.gov).

Minghui Zheng is with the Department of Mechanical and Aerospace Engineering, University at Buffalo, Buffalo, NY 14260 USA (e-mail: mhzheng@buffalo.edu).

This article has supplementary material provided by the authors and color versions of one or more figures available at https://doi.org/10.1109/TRO.2022.3170287.

Digital Object Identifier 10.1109/TRO.2022.3170287

8.60%-15.22% relative to the unpowered condition and two knee flexors and one ankle plantar flexor by 1.92%-10.24% relative to the baseline (no exoskeleton) condition.

*Index Terms*—Force/torque control, knee exoskeleton, quasi-direct-drive actuation, stiffness control.

#### I. INTRODUCTION

PORTABLE lower-limb exoskeletons have great potential for mobility restoration and human augmentation [1]–[3]. Compliance, low mass, and the ability to assist a diverse array of movements are key requirements for an exoskeleton to be viable in daily life. There is a wealth of literature on ankle exoskeletons to augment human walking [4]–[7] and a substantial amount of literature on hip or ankle exoskeletons for walking augmentation [8]–[13]. Comparably, there is little research study on knee exoskeletons for augmentation [14], [15], likely because the positive work done at the knee in level walking is less than that at the ankle or hip [16]. However, the knee is crucial in locomotion, and there is a compelling need to investigate the benefits of a knee exoskeleton on human performance and understand the human–robot interaction.

The challenges of exoskeleton design stem from the need to balance multiple attributes of the mechatronic system, including weight, power, and compliance, while being able to replicate near biological levels of assistance [1], [17]. Tethered actuation can circumvent the exoskeleton design challenges in a research environment, but tethered exoskeletons are not directly transferable to real-world applications. Untethered (or portable) exoskeletons are suitable for noncontrolled environments and have a wide potential for mobility assistance [18] and human augmentation [11]. But the mass of the actuators, power supply, and wearable structure imposes a penalty on energetics and biomechanics that some state-of-the-art exoskeletons have not managed to overcome [19], [20]. Furthermore, these exoskeletons are not very compliant, which can inhibit natural movements [19]. The most prevalent method of enhancing compliance is to use a series elastic actuator (SEA), which introduces a spring, an elastic element of fixed stiffness [21]. In addition, variable stiffness actuators (VSA) can vary stiffness throughout gait but typically require a second motor [22]. Both SEA and VSA bring extra weight and make the exoskeleton heavy and bulky. A further difficulty in using series elastic or VSA in exoskeletons is their low bandwidth, making it challenging to adapt

1552-3098 © 2022 IEEE. Personal use is permitted, but republication/redistribution requires IEEE permission. See https://www.ieee.org/publications/rights/index.html for more information.

Unilateral Knee Exoskeleton	Weight (kg)	Actuation Paradigm	Gear Ratio	Actuation Torque (Nm)	Actuation Reflected Inertia (kg-cm2)	Torque Density (Nm/kg)	Backdrive Torque (Nm)	Torque Control Bandwidth (Hz)	Control Method
This work	2.1	QDD	6:1	14	32.22	6.66	Low (0.22)	High (40.7)	State-based
Zhu [29]	2.69	QDD	7:1	10.5	200.90	3.90	Low (1.32)	High (55.1)	Phase angle
Lee [20]	2.7	Conventional	113:1	15.14	2311.19	5.61	Medium	Medium	Time-based
Chen [40]	2.59	Conventional	153:1	14.63	772.50	5.65	Medium	Medium (9.6)	Time-based
Karavas [19]	>41	SEA	100:1	81.3	39320.00	N/A	High	Low	EMG-based
Liu [41]	>51	SEA (VSA)	100:1	45.8	31700.00	N/A	High	Low	N/A

TABLE I COMPARISON OF PORTABLE KNEE EXOSKELETONS

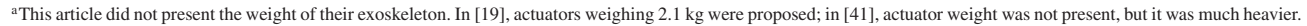




Fig. 1. Lightweight and compact powered portable knee exoskeleton is based on QDD actuation. The knee exoskeleton comprises a waist belt, an adjustable elastic strap, a thigh support frame, a knee joint actuation system, and a shank support frame. The total weight of a middle-size unilateral (bilateral) knee exoskeleton is 2.1 (3.5) kg, including control electronics and battery (0.7 kg).

the assistance to human locomotion or unexpected perturbations [23], [24]. Thus, SEA actuators are not able to realize both high compliance and high bandwidth, and there is a solid need to overcome this limitation. Except for electric motors, a compliant exoskeleton with pneumatic artificial muscles was studied in [25] and [26], but both the bandwidth and stiffness range are minimal, and the artificial muscles must be tethered to a large and heavy air compressor.

To address the multifaceted mechatronic design challenges of exoskeletons, we proposed a quasi-direct-drive (QDD) actuator with electrically adjustable stiffness in this article. QDD actuators, comprised of high-torque-density motors and low gear ratio transmission, were popularized in legged robots [27], [28] before they gained traction in the wearable robotics community [23], [29], [30]. Our prior work [23] focused on the mechatronics design of a hip exoskeleton, but this work is primarily about novel control algorithms for knee exoskeletons. Compared with the QDD actuator used in the legged robot [28], our actuator contains a customized motor with a high torque constant. Therefore, our actuator has a high torque density, and it meets the high-torque and lightweight requirements of knee exoskeleton applications. As shown in Fig. 1, by leveraging our high-torquedensity actuator and simple mechanical design (e.g., no spring mechanism and associated structures), we developed the most lightweight, portable powered knee exoskeleton (see Table I),

which is the platform to study stiffness modeling and continuous torque control in this article. To the best of our knowledge, there is no investigation into the stiffness control of QDD actuators for wearable robots to understand the performance through modeling and experiments. The low-inertia and high-stiffness transmission of QDD actuators can be designed with a high stiffness control bandwidth with a large range of stiffness, making them uniquely suitable for exoskeletons.

Traditional high-level exoskeleton controllers cannot accurately produce biological joint moment patterns and adapt to changes in walking patterns [20], [31]. Existing exoskeleton controls are typically based on time (gait cycle) [32] or kinematics (e.g., joint angle) [33]. Those controllers typically implement the assistive torque profile for discrete phases of the gait cycle and have difficulty adapting to varying walking patterns (e.g., speed changes and sudden stops), because the assistive torque profile can only be changed at the start of the following discrete segment.

Therefore, continuous gait detection and controllers are gaining popularity in wearable robotics. They can instantaneously update the assistance profile in response to the input signal (e.g., joint angle), which allows quick adaptations to change in the walking pattern [34]-[37]. Martinez et al. [34] used hip and knee joint angles to map joint kinematics to drive torque control for a lower-limb exoskeleton in the swing phase and allow the user to change step length and step time. Lim et al. [35] used hip joint angle to provide continuous sinusoidal torque assistance at the hip exoskeleton. Quintero et al. [36] used the gait phase to map kinematics constraints to continuously provide periodic (sine and cosine)-wave-based torque assistance for a knee-ankle prosthesis. However, none of them can generate continuous biological torque profiles. Thatte et al. [37] developed a continuous torque profile to assist knee-ankle prosthesis by utilizing joint angle, angular velocity, and feedforward torque. However, this method is computationally expensive, and the angular velocity data from the differential calculation make the controller sensitive to noise from ground contacts [36].

To continuously provide proportional biological torque assistance, we developed a stiffness-based continuous torque controller in this article. As one type of impedance control, stiffness control (no inertia and damper terms, no acceleration, and angular velocity data required) can be a simple yet robust control method to produce mechanical compliance for assistive wearable robots. The biomechanics of human walking involves the coordination of lower-limb joints with complicated

stiffness dynamics [15], [38]. It is of great significance if the wearable robot can provide sufficient stiffness dynamics for handling various human movement patterns. However, reported stiffness control methods for the assistive wearable robot are generally either discrete or discontinuous [39]. Inspired by the gait biomechanics, we propose a simple stiffness-torque model for our stiffness-based continuous torque controller to estimate biological moment in real-time using only a few measurements (i.e., knee joint angles). There are several advantages of this work. First, looking at the torque assistive control from a statespace perspective ensures that our controller is not too sensitive to errors in timing. Second, a controller based on the estimated biological knee moment provides a broadly applicable assistance model that does not depend on a particular angle/trajectory but instead allows the assistance to be scaled as a percentage of user effort (i.e., volitional moment). This approach can be used for augmentation (the focus of this article), whereby the amount of assistance can be proportional to the effort exerted by the user. Likewise, the same approach can be beneficial for rehabilitation by ensuring that a targeted amount of volitional effort (or muscle activity) is maintained.

This work focuses on two major contributions by leveraging our lightweight exoskeleton platform. First, we developed a stiffness model of QDD exoskeleton and benchmarked it with the series-elastic-actuation-based exoskeletons. The results showed that our exoskeleton (see Fig. 1) has a high stiffness control bandwidth (16 Hz under 100 N·m/rad) with a large range of stiffness (our robot provides 0–350 N·m/rad stiffness compared to the human knee joint stiffness of 0-176 N·m/rad) and high torque tracking accuracy [root-mean-square (rms) error of 0.34 N·m, 6.22% of the desired peak torque]. Second, we proposed a continuous torque controller that uses the stiffness model to estimate the biological torque in real-time and is computationally efficient and adaptable to different overground walking speeds to overcome the limitations of discrete controllers (e.g., finite-state machine methods). The results of eight able-bodied subjects indicated that our proposed exoskeleton could reduce the rms muscle activation of all the eight measured knee and ankle muscles by 8.60%–15.22% compared to the unpowered condition. A reduction of 1.92%–10.24% in rms muscle activities of two knee flexors and one ankle plantar flexor in eight able-bodied subjects compared with the baseline condition.

# II. BIOMECHANICS OF HUMAN KNEE DURING WALKING AND REQUIREMENTS FOR DESIGN AND CONTROL

Understanding the biomechanics of human knees is crucial to enabling symbiotic human–robot collaboration. Specifically, it involves creating high-performance mechatronics, deriving models of human–robot interaction, and developing bioinspired control.

### A. Biomechanics of the Human Knee During Walking

The knee is essential for efficient locomotion, supporting body weight, absorbing shock, and providing foot clearance. The angle, moment, and power of the joint describe the action and

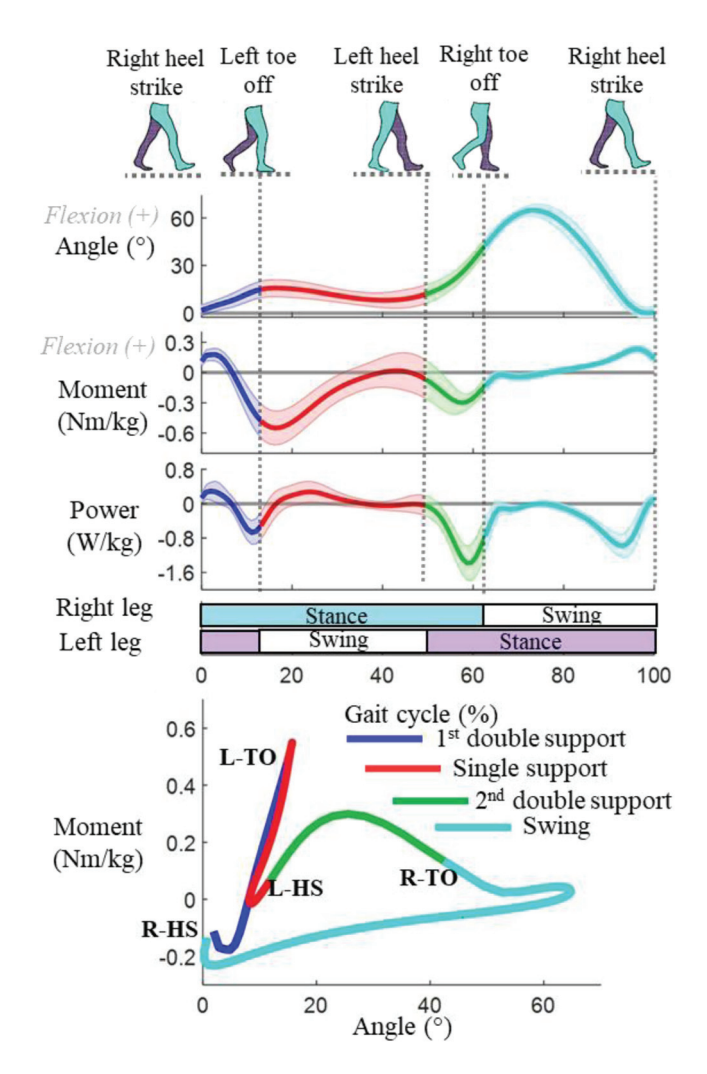


Fig. 2. Knee biomechanics over a stride. Shaded areas represent the standard deviation. Different colors indicate the four phases: initial double support, single support, second double support, and swing.

function of the knee. The piecewise linear moment–angle relationship (also called quasi-stiffness) of the knee is a measure that characterizes knee stiffness and essentially models the knee joint as a torsional spring in distinct phases of stride [42]. Fukuchi *et al.* [43] collected biomechanics data from 23 subjects walking on a level treadmill at  $1.24 \pm 0.05$  m/s and found an average peak torque of 31 N·m (0.46 N·m/kg) and the quasi-stiffness ranging from 0 to 176 N·m/rad.

As illustrated in Fig. 2, each stride can be split into the following four phases:

- 1) initial double support;
- 2) single support;
- 3) second double support;
- 4) swing phase.
- 1) Initial Double Support: The body weight is transferred from the trailing limb (left) to the leading limb. The knee joint moment–angle relationship is very linear in this phase, and the quasi-stiffness is high.
- 2) Single Support: The right leg supports the entire body weight in this phase. The moment–angle relationship is linear

in this phase, with a similar quasi-stiffness to the initial double support.

- 3) Second Double Support: The body weight is shifted from the right leg to the left leg in this phase. The knee moment– angle relationship is somewhat linear in this phase, although the quasi-stiffness is substantially lower than in the previous phases.
- 4) Swing Phase: The knee flexes to assist with foot clearance and then extends in preparation for ground contact. Overall, the moment magnitude in the swing phase is lower than in the stance phase. Although the relationship is nonlinear (especially around the transition from flexion to extension), most of the phase can be represented as linear with relatively small error due to the low moment magnitude.

The benefits of powered assistance to the knee joint are not well understood. One reason is that state-of-the-art powered knee exoskeletons are heavy, and the mass penalty affects natural movements [41]. There is no prior work to systematically investigate the effects of a powered portable knee exoskeleton in three conditions (powered, unpowered, and baseline without exoskeleton). Although the knee contributes less positive power than the ankle and hip joints in level walking [16], [44], the knee is vital for effectual walking. And it is beneficial for the knee to have external assistance. First, some of the muscles that actuate the knee joint are multiarticular, meaning the muscle crosses and actuates multiple joints simultaneously [45]–[47]. Augmenting the knee joint will affect the muscle biomechanics of the bi- and triarticular muscles, which could improve muscle efficiency or network efficiency done at the joint. Second, studies have found that altering dynamics at one lower-limb joint can modify the dynamics of the nonassisted joints, such that a knee exoskeleton may be able to improve walking or muscle efficiency not only at the knee joint but also at the ankle and hip joints [15], [48], [49]. Third, modern inverse dynamics techniques (using six degrees of freedom) found that traditional inverse dynamics (with three degrees of freedom) underestimated the positive work done at the knee. Thus, more positive work was done at the knee than reported in the biomechanical study [50]. The powered knee exoskeleton could potentially benefit the wearer by increasing the amount of positive work done at the knee. In addition to these energetic considerations, a knee exoskeleton that reduces load through the knee has the potential to prevent injury, reduce chronic pain, or improve the walking ability of people with musculoskeletal impairments [51]–[55].

## B. Requirements for Design and Control

Portable exoskeletons should be lightweight to reduce the energetic penalty of wearing the exoskeleton and diminish impacts on the inertial properties of legs [56]. For our design, we set desired parameters such that it exceeds the performance defined by knee biomechanics at 1.25 m/s walking speed to ensure the versatility of the exoskeleton, e.g., providing assistance across different walking speeds and not impeding natural movements (e.g., squatting and stair climbing). The requirements are summarized in Table II. Exoskeleton joint stiffness is required to span the range of biological stiffness (0–176 N·m/rad). It is

TABLE II
DESIGN PARAMETERS OF THE KNEE EXOSKELETON

Parameters	Human Walking	Desired	This work
Knee flexion (°)	65	130	130
Range of knee joint stiffness (Nm/rad)	0 - 176	0 - 200	0 - 350
Max knee joint moment (Nm/kg)	0.4	0.12	0.25
Max knee joint speed (rad/s)	6.63	10	25
Exoskeleton weight (kg)		5	3.5

unnecessary to provide assistive torque equivalent to 100% biological torque because well-timed assistive torques (e.g., 30%) can impart substantial biomechanical benefits to able-bodied individuals [30], [57]. Prior study on knee exoskeletons has predominantly focused on assisting only during the stance phase [15], [18], [20], as most mechanical work of a knee occurs in this phase. Swing-phase knee assistance is primarily used for rehabilitation or assistance to users with limited mobility [52], [53]. Lockheed Martin's Onyx is one of the few knee exoskeletons for able-bodied augmentation that provides assistance in both the stance and swing phases for level-ground walking [14]. Augmenting the knee during the swing phase would help compensate for the added mass on the leg, which needs to be carried through the swing phase. Furthermore, assisting the knee during the swing phase may also improve dynamics at the ankle or hip joint. Therefore, we chose to assist the entire stride.

For stiffness control of knee exoskeletons, state-of-theart robots typically use discrete quasi-stiffness models [21], usually facilitated by finite-state machines [39]. Aguirre-Ollinger *et al.* [21] recently developed an SEA actuation that operated between two discrete stiffness levels. However, discrete stiffness controllers tend to have large torque jerks between different stiffness modes, resulting in disruptive discontinuities in the assistance profile. One novelty of our work is a continuous stiffness controller based on the quasi-stiffness model of the knee joint, which provides a smoother and more natural assistance profile than switching among discrete stiffness values.

# III. MECHATRONIC DESIGN OF A PORTABLE KNEE EXOSKELETON WITH QDD ACTUATION

In this section, we present the mechatronic design of a portable knee exoskeleton by leveraging our custom high-torque-density motor and low gear ratio transmission for QDD actuation. This platform is the foundation for the two contributions of this work, namely, stiffness modeling of a torque-controlled QDD exoskeleton and continuous torque control.

### A. QDD Actuation

To meet the design and control requirements, our actuator is designed to be lightweight, compliant, and with a high bandwidth. Leveraging our high-torque-density motor [23], [24] and gear-embedded actuator design method [28], we customize a compact QDD actuator with fully integrated control electronics components (see Fig. 3). The actuator is lightweight (485 g) and compact ( $\Phi100~\text{mm}\times37~\text{mm}$  height) and can generate

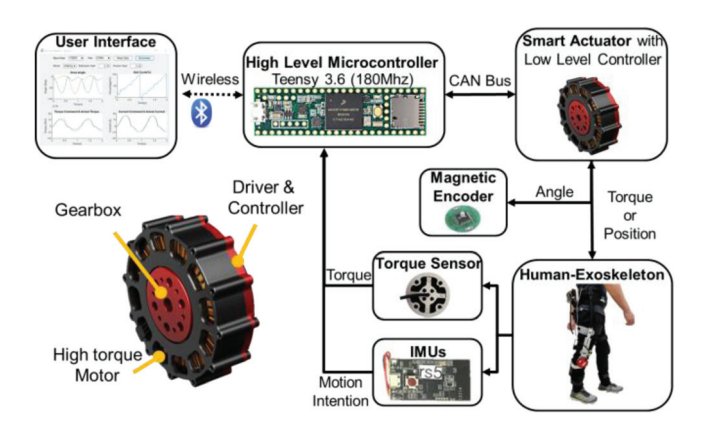


Fig. 3. Electronic hardware architecture and QDD actuator (6:1 planetary gear) of the knee exoskeleton. The fully integrated architecture of the actuator includes a motor, a gearbox, and control electronics. We implement high-level control with a Teensy microcontroller. The robot could wirelessly communicate with a remote PC for data logging.

20 N·m peak torque. The actuator includes a custom high-torque-density brushless direct current motor with 3.3 N·m peak torque output capability, an embedded 6:1 ratio planetary gear, a 14-b magnetic encoder (AS5048A, AMS, USA), and a microcontroller (STM32F407, STMicroelectronics, France). Unlike SEA actuators that use a high-gear-ratio mechanism (e.g., a harmonic driver) and a spring mechanism, QDD actuators are based on a low gear ratio without spring components. Thus, QDD actuators are generally simpler and more affordable in terms of mechatronics design.

We implement a low-level control loop in the motor microcontroller to realize position, velocity, and current control. Real-time communication with a high-level control device is executed through the controller area network bus protocol. Powered by a nominal voltage of 42 V, the actuator reaches a nominal speed of 250 r/min (26.17 rad/s). Moreover, thanks to the low gear ratio transmission of the QDD design, the actuator has low output inertia (32.2 kg·cm², see Table I for benchmark comparison with other exoskeletons), which is crucial to achieving low impedance that minimizes the resistance to human natural movements.

### B. Mechatronic Design of Knee Exoskeleton

The design principle of this knee exoskeleton is to ensure a natural range of motion for multiple locomotion activities, e.g., walking, squatting, and stair ascent (lightweight and compliant features) and to minimize interference with external environments (compact feature). Thus, the design avoids complicated mechanisms (e.g., our early work [58] that used a double-rolling mechanism for the knee exoskeleton). The main components of the exoskeleton include a waist belt, an actuation system, thigh and shank support frames, and an adjustable elastic strap (see Fig. 1). The knee joint actuation system includes a QDD actuator and a custom torque sensor ( $\pm$  40 N·m full scale and  $\pm$  0.1 N·m resolution). The QDD actuator is connected to the thigh support frame, and the load cell is connected to the shank support frame. The design of the cuffs and straps ensures the assistive force on

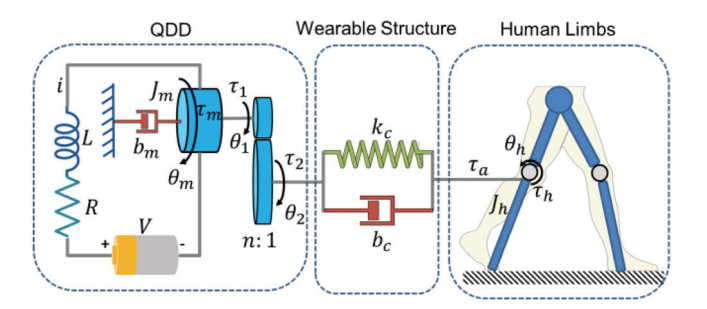


Fig. 4. Model of the coupled human–knee exoskeleton system. It includes a QDD actuator, wearable structures, and human limbs (represented by the blue bars).

the wearer's thigh and shank is perpendicular to the surface of the respective segment, which reduces shear forces and discomfort.

We design the knee exoskeleton with the potential to assist multiple movements and for people with different body shapes. The wearable structures of the anterior lower thigh and shank do not interfere at maximum flexion (e.g., deep squatting). The range of motion of the knee exoskeleton is 0°–160° (flexion), which is compatible with activities that require a wide range of motion, like stair ascent, sit-to-stand, and squatting. Additionally, different sizes of wearable structures are available. When combined with the adjustable linkage and single-hinge structure, the design ensures the knee exoskeleton could fit a wide range of body sizes. The unilateral knee exoskeleton (without waist belt and battery) weighed 1.4 kg. The total weight of the bilateral knee exoskeleton (including all components) is 3.5 kg.

The electronic architecture of the knee exoskeleton facilitated high-level torque control, motor control, sensor signal conditioning, data communication, and power management, as shown in Fig. 3. The low-level controller embedded in the smart actuator measures the motor motion to realize motor current, velocity, and position control. The high-level microcontroller runs on Teensy 3.6 and implements continuous torque control (see Section V). The microcontroller acquires knee joint angles from two wireless inertial measurement units (IMU) sensors of each limb and conditioned torque signals from the custom loadcells in real-time. A Bluetooth microcontroller (nRF52840 Express, Adafruit, USA) connected to the main controller acts like a transceiver to communicate with a remote desktop computer for real-time data logging and monitoring.

### IV. STIFFNESS MODELING AND BENCHMARK OF TORQUE-CONTROLLED QDD EXOSKELETON

To demonstrate that the QDD knee exoskeleton has the potential to achieve human walking stiffness, we proposed a stiffness control model of the torque-controlled exoskeleton to benchmark QDD actuation exoskeletons. The effects of design parameters on the stiffness control bandwidth and range are then analyzed.

The model of the human–knee exoskeleton system (see Fig. 4) incorporates the electromechanical model of the QDD actuator, the impedance model of the human–exoskeleton interface, and the biomechanical model of human walking [23].  $V, L, R, i, J_m$ ,

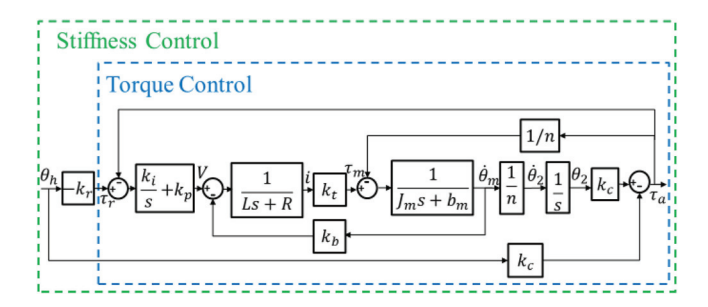


Fig. 5. Block diagram of the stiffness controller. The input is the human knee angle  $\theta_h$  and the output is the assistive torque  $\tau_a$  at the knee joint. The controller aims to achieve the desired stiffness value of the exoskeleton by generating the corresponding torque reference  $\tau_r$ . Here, the I gain is set to zero to simplify the benchmark comparison.

 $\theta_m, \tau_m, b_m, \tau_1, \theta_1, n, \tau_2, \theta_2, k_c, b_c, \tau_a, \tau_h, J_h$ , and  $\theta_h$  denote the winding voltage, winding inductance, winding resistance, motor current, motor rotor inertia, motor angle, motor input torque, motor damping, motor output torque, gear input angle, gear ratio, gear output torque, gear output angle, human—exoskeleton transmission stiffness, human—exoskeleton transmission damping, exoskeleton output assistive torque, knee muscle torque, human shank inertia, and knee angle, respectively.

We hypothesize that the QDD actuation paradigm has a higher control bandwidth and a larger range of stiffness than conventional (CON) and SEA actuation because of the high-torquedensity motor, low gear ratio, and high stiffness transmission. To test our hypothesis, we use a human–exoskeleton model to derive the continuous stiffness control model and characterize the performance of knee exoskeletons with CON, SEA, and QDD actuation paradigms.

# A. Torque Control Modeling of Human–Exoskeleton Interaction

As discussed in Section II, a variable stiffness model can capture the dynamics of the human knee joint during walking. Here, we propose stiffness control to generate the torque for knee assistance with the QDD actuation paradigm. As shown in Fig. 5, the inner loop is the torque control, in which the input is the torque reference  $\tau_r$  and the output is the actual torque applied to the human shank. In the model, the transmission damping coefficient  $b_c$  is small and set to zero;  $k_p$  and  $k_i$  are the proportional and integral gains, respectively. In this work, we derive the stiffness model and investigate stiffness dynamics by analysis (see Section IV-B) and experiments (see Section VI-A).

### B. Stiffness Model of Torque-Controlled Exoskeletons and Benchmark of Three Actuation Paradigms

To establish the stiffness model, the input torque reference is given by

$$\tau_r = -k_r \theta_h \tag{1}$$

where the torque reference  $\tau_r$  is generated proportionally to the knee angle  $\theta_h$  via the reference stiffness  $k_r$ . The transfer function for joint stiffness is modeled by

If we consider the motor inductance L to be approximately zero, then (2) is reduced to

$$k_{\text{stiffness}}(s) |_{L=0} = \frac{-\tau_a(s)}{\theta_h(s)} |_{L=0}$$

$$= \frac{k_c \left[ n^2 J_m R s^2 + n^2 \left( R b_m + k_b k_t \right) s + n k_p k_r k_t \right]}{\left\{ n^2 J_m R s^2 + n^2 \left( R b_m + k_b k_t \right) s + \left( R k_c + n k_c k_p k_t \right) \right\}}. \quad (3)$$

To investigate the bandwidth of the stiffness control, the first and second corner frequencies (the corner frequency is defined as the boundary where frequency response begins to be attenuated or amplified) of the closed-loop stiffness control are found in (4). Because the transmission stiffness  $k_c$  and torque constant  $k_t$  of the QDD system are larger and the gear ratio n is smaller than those of the SEA system (see Table IX), the corner frequency of the stiffness control will be larger with the QDD system than in SEA and CON high gear ratio actuation

$$\omega_1, \ \omega_2 = \sqrt{\frac{nk_rk_pk_t}{n^2J_mR}} \ , \ \sqrt{\frac{k_c\left(R + nk_pk_t\right)}{n^2J_mR}}. \tag{4}$$

To investigate the stiffness tracking performance in the frequency domain, the transfer function is given by

$$k_{\text{stiffness}}(j\omega)|_{L=0} = \frac{-\tau_a(j\omega)}{\theta_h(j\omega)}|_{L=0}$$

$$= \frac{k_c \left[ -n^2 J_m R \omega^2 + n^2 \left( R b_m + k_b k_t \right) \omega j + n k_r k_p k_t \right]}{\left\{ -n^2 J_m R \omega^2 + n^2 \left( R b_m + k_b k_t \right) \omega j + \left( R k_c + n k_c k_p k_t \right) \right\}}.$$
(5)

Considering that human motion is characterized by low frequency ( $\omega \to 0$ ), the system stiffness is represented as follows:

$$\lim_{\omega \to 0} k_{\text{stiffness}} (j\omega) |_{L=0} = \frac{k_c n k_r k_p k_t}{R k_c + n k_c k_p k_t}.$$
 (6)

Additionally, when  $k_p$  is large enough, such that  $k_p \to \infty$ , the system stiffness can be approximated by  $k_r$ , i.e.

$$\lim_{\omega \to 0, \ k_p \to \infty} k_{\text{stiffness}} \left( j\omega \right) |_{L = 0} = k_r \tag{7}$$

which indicates that the stiffness controller can accurately track the reference stiffness  $k_{\scriptscriptstyle T}$  for low-frequency human motion.

Conversely, when the motion frequency is high  $(\omega \to \infty)$ , the transfer function approximates the transmission stiffness  $k_c$ , i.e.

$$\lim_{\omega \to \infty} k_{\text{stiffness}} (j\omega) |_{L=0} = \frac{k_c n^2 J_m R \omega^2}{n^2 J_m R \omega^2} = k_c.$$
 (8)

Therefore, the stiffness controller cannot track the reference stiffness  $k_r$  in high-frequency motion. Our QDD exoskeleton can provide sufficient bandwidth for dynamic stiffness tracking.

To illustrate the performance of stiffness control, the transfer function in (2) is depicted in the Bode diagram in Fig. 6. We use the derived stiffness control model (8) to benchmark the following three actuation methods:

- 1) a CON high-gear-ratio knee exoskeleton [59];
- 2) an SEA-based knee exoskeleton [60];
- 3) our ODD knee exoskeleton.

The SEA and CON have a higher ratio gear than the QDD actuation, and the SEA has a low stiffness constant due to the

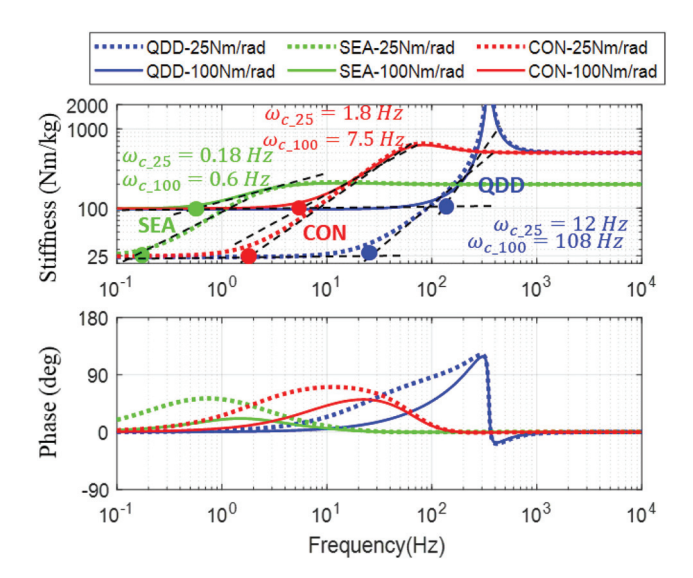


Fig. 6. Bode diagram of stiffness control for three actuation methods through the model derived in (2)–(8). The input is the human knee angle  $\theta_h$ , and the output is the calculated torque  $\tau_a$  (negative value, opposite to the rotation direction). The magnitude of the Bode diagram is the calculated joint stiffness. The QDD has the highest bandwidth compared to SEA and CON actuators because of the high transmission stiffness and low gear ratio. Since human motion is characterized by low frequency, our QDD exoskeleton could have sufficient bandwidth for dynamic stiffness tracking in both low- and high-stiffness conditions.

mechanical spring. For simplicity of the benchmark comparison, we set a large transmission stiffness of 500 N·m/rad for the CON and QDD actuators and a small transmission stiffness of 200 N·m/rad for the SEA. The parameters from these three representative knee exoskeletons are listed in Table IX in the Appendix.

The bandwidths of the stiffness control for the QDD, SEA, and CON actuation with 25 N·m/rad reference stiffness are approximately 12, 0.18, and 1.8 Hz, respectively. The bandwidths of the stiffness control with 100 N·m/rad reference stiffness for the QDD, SEA, and CON are approximately 80, 0.6, and 7.5 Hz, respectively. These results show that the QDD has the highest stiffness bandwidth at both 25 and 100 N·m/rad. At high frequencies, the actuator stiffness is dominated by the transmission spring stiffness  $k_c$ . Therefore, the actual stiffness of the SEA, CON, and QDD at a high frequency (see the stiffness in Fig. 6 as the frequency approaches  $10^4$  Hz) is approximated as  $k_c$ .

### V. STIFFNESS-BASED CONTINUOUS TORQUE CONTROL

### A. Architecture of High and Low-Level Controllers

The main objective of the control law is to estimate the biological knee moment continuously during walking and assist the subject with a torque profile proportional to the estimated biological moment. Traditional finite-state machine control methods, such as those presented in [42], [56], and [61], are composed

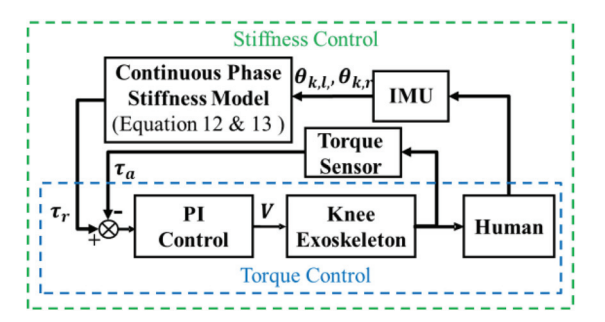


Fig. 7. Architecture of the stiffness-based continuous torque control. It consists of two levels: 1) The stiffness control is the outer loop and 2) the torque control is the inner loop.  $\theta_{k,l}$  and  $\theta_{k,r}$  represent the right and left knee angles, respectively,  $\tau_r$  is the reference torque estimated by the continuous-phase stiffness model, and  $\tau_a$  is the measured torque from the torque sensor.

of two steps: 1) the gait cycle or phase-detection algorithm and 2) assistive torque generation in terms of the gait phase of the gait cycle. Therefore, for different gait phases [40], the generated torque profiles are discontinuous, and the accuracy of assistive torque is dependent on the accuracy of gait phase detection. To overcome the problem of inaccurate gait phase estimation and discontinuous stiffness-based torque assistance (e.g., piecewise quasi-stiffness torque profiles), we develop a continuous-stiffness model to estimate the knee joint moment. Our real-time control method combines gait phase detection and knee joint moment estimation into a unique estimation model, which identifies both the instantaneous gait phase and the required stiffness through an optimization process.

In Section II, we note that the knee joint quasi-stiffness transitioned between a high stiffness in the stance phase and low stiffness in the swing phase. The proposed control scheme is shown in Fig. 7. The variable stiffness control generated by the continuous-phase stiffness model is employed as the high-level controller, which is given by

$$\tau_r = k_a \ k_w \hat{\tau}_{k,r} \tag{9}$$

where  $\tau_r$  is the reference torque of the variable stiffness control,  $\hat{\tau}_{k,r}$  is the normalized estimated knee moment (described in Section IV-B),  $k_w$  is the user's body weight (in kg), and  $k_a$  is the assistive proportional gain. The inputs of the variable stiffness control are the right knee angle  $\theta_{k,r}$  and left knee angle  $\theta_{k,l}$ . The output is the torque reference  $\tau_r$ . The control law for knee assistance can be calculated from (9). Assistive control is achieved with a  $k_a$  in the range [01]. We use IMUs on each shank and thigh (two IMUs of each leg) to calculate the right and left knee angles ( $\theta_{k,r}$  and  $\theta_{k,l}$ , respectively). The inner-loop controller implements torque control, and the feedback signal is the measured assistive torque  $\tau_a$  (measured from the torque sensor of the knee exoskeleton).

$$k_{\text{stiffness}}\left(s\right) = \frac{-\tau_{a}\left(s\right)}{\theta_{h}\left(s\right)} = \frac{k_{c}\left[n^{2}J_{m}Ls^{3} + n^{2}\left(J_{m}R + Lb_{m}\right)s^{2} + n^{2}\left(Rb_{m} + k_{b}k_{t}\right)s + nk_{r}k_{p}k_{t}\right]}{\left\{n^{2}J_{m}Ls^{3} + n^{2}\left(J_{m}R + Lb_{m}\right)s^{2} + \left[n^{2}\left(Rb_{m} + k_{b}k_{t}\right) + Lk_{c}\right]s + \left(Rk_{c} + nk_{c}k_{p}k_{t}\right)\right\}}.$$
 (2)

# B. Stiffness-Based Continuous Torque Controller With Biological Torque Estimation

We propose a simple and analytical model that uses a smooth function (e.g., sigmoid function) to generate a continuous output between 0 and 1, which is given by

$$S(\theta_{k,r}, \theta_{k,l}) = \frac{1}{1 + e^{-af(\theta_{k,r}, \theta_{k,l})}}.$$
 (10)

The parameters a could regulate the width of the transition area of the sigmoid function. The function  $S(\theta_{k,r},\theta_{k,l})$  is the likelihood to apply the swing-phase stiffness model. The function  $[1-S(\theta_{k,r},\theta_{k,l})]$  is the likelihood to apply the stance-phase stiffness model. The continuous nature of the gait phase detection output ensures that the estimation of the knee moment is also a continuous signal. An additional benefit of continuous gait phase detection is that transitions between gait phases can be easily and automatically processed instead of rule-based methods like a finite-state machine. The proposed estimation function is given by

$$\hat{\tau}_{k,r} = [1 - S(\theta_{k,r}, \theta_{k,l})] k_{st} (\theta_{k,r} - \theta_{k,st,0})$$

$$+ S(\theta_{k,r}, \theta_{k,l}) k_{sw} (\theta_{k,r} - \theta_{k,sw,0})$$

$$(11)$$

where  $S(\theta_{k,r}, \theta_{k,l})$  is the sigmoid function given by (10),  $\hat{\tau}_{k,r}$  is the estimation of the right knee moment,  $k_{\rm st}$  is the joint stiffness of the stance phase,  $k_{\rm sw}$  is the joint stiffness of the swing phase,  $\theta_{k,r}$  is the right-limb knee angle,  $\theta_{k,l}$  is the left-limb knee angle,  $\theta_{k,r,0}$  is the equilibrium angle for the stiffness model of the stance phase,  $\theta_{k,st,0}$  is the equilibrium angle for the stiffness model of the stance phase, and  $\theta_{k,sw,0}$  is the equilibrium angle for the stiffness model of the swing phase. Here, we propose to use two stiffness modes (high stiffness and low stiffness) to estimate the knee moments  $\tau_{k,r}$  and  $\tau_{k,l}$ . In addition, the proposed method is not limited to stiffness control. It can be extended to a higher-order model of a generic impedance controller with mass, spring, and damper terms, which needs angular velocity and angular acceleration (the derivatives of the knee angle and angular velocity, respectively). When implemented, the differential operation for the angular acceleration and angular velocity generates a noncausal system and introduces noise. Therefore, we choose to use stiffness control (without angular velocity and angular acceleration) that requires only joint angle feedback to approximate the knee moments  $\tau_{k,r}$  and  $\tau_{k,l}$ .

The estimated optimal hyperplane is given by

$$f\left(\theta_{k,r},\ \theta_{k,r}\right) = \left(\theta_{k,r} - \theta_{k,l}\right) - b \tag{12}$$

minimize 
$$\sum_{i=0}^{m} (\hat{\tau}_{k,r,i} - \tau_{k,r,i})^{2}.$$
 (13)

Equation (12) separates the gait cycle into two gait phases by minimizing the torque estimation error. The parameter b could regulate the center of the transition area of the sigmoid function. The only input variables required to estimate the gait phase are right- and left-limb knee angles ( $\theta_{k,r}$  and  $\theta_{k,l}$ , respectively). Hence, this control law is more stable compared to gait estimation methods that use angular velocity and/or acceleration. The

TABLE III
OPTIMAL PARAMETERS FOR THE CONTINUOUS-PHASE STIFFNESS MODEL

Parameter	$k_{st}$	$\theta_{k,st,0}$	$k_{sw}$	$\theta_{k,sw,0}$	а	b
Coefficient	0.0379	5.322	0.0046	57.520	0.099	2.619

TABLE IV CORRELATION RESULTS OF THE CONTINUOUS-PHASE STIFFNESS MODEL

Dataset	Dataset Slow	Dataset Self-selected	Dataset Fast	Average
Correlation	80.9%	96.1%	94.5%	90.0%

output of the estimation function (11) is the estimated right knee moment  $\hat{\tau}_{k,r}$ .

To find the optimal parameters  $(k_{\rm st}, k_{\rm sw}, \theta_{k, {\rm st}, 0}, \theta_{k, {\rm sw}, 0}, a, {\rm and})$ b) of the continuous-phase stiffness model (see Fig. 7), we solve an offline optimization problem over a collection of training data from 23 subjects walking overground [43]. Each subject was asked to perform overground walking trials at three speeds (a self-selected comfortable speed, a fast speed, which is 30% faster than the self-selected speed, and a slow speed, which is 30% slower than the self-selected speed. The dataset for each speed includes the averaged knee joint angles and moments from multiple trials. The time series of the data is converted to the percentage of the gait cycle, and the joint moment is normalized to body mass (N·m/kg). We use the data at all three walking speeds to optimize the stiffness model parameters. Specifically, nonlinear regression is used to minimize the sum of the squared error between the estimated and actual knee moments, employing the cost function in (13). Here,  $\hat{\tau}_{k,r,i}$  and  $\tau_{k,r,i}$  are the estimated and actual knee moments at data point i, respectively, whereas parameter m is the total number of data points in the training data. In this way, a nonlinear regression method is able to optimize parameters, including the width of the transition area (parameter a), the stiffness ( $k_{st}$  and  $k_{sw}$ ), and the equilibrium angles  $(\theta_{k,\text{st},0} \text{ and } \theta_{k,\text{sw},0})$  of the two-phase stiffness models. The optimal hyperplane  $f\left(\theta_{k,r},\theta_{k,l}\right)=0$  separates the gait cycle into two gait phases (corresponding to  $f(\theta_{k,r}, \theta_{k,l}) = 0$ ) to minimize the error between the estimated biological moment and the actual biological moment.

# C. Optimization of Biological Torque Estimation for Continuous Stiffness Torque Control

Optimal parameters of the continuous-phase stiffness model are shown in Table III. The hyperplane (in the space of the angle difference between the right and left knee joints) is close to zero degree.

In our exoskeleton control law, the assistive torque is proportional to the estimated knee moment. We evaluate the accuracy of the estimated torque with respect to the actual knee moment using the correlation between the actual knee joint moment and the moment estimated by the continuous-stiffness model at the three different walking speeds (see Table IV). The average correlation is 90%. The highest correlation (about 94.5%) is found in the comfortable walking condition, whereas the slow-walking-speed data has the lowest correlation (80.9%). These results indicate that the proposed joint moment estimation

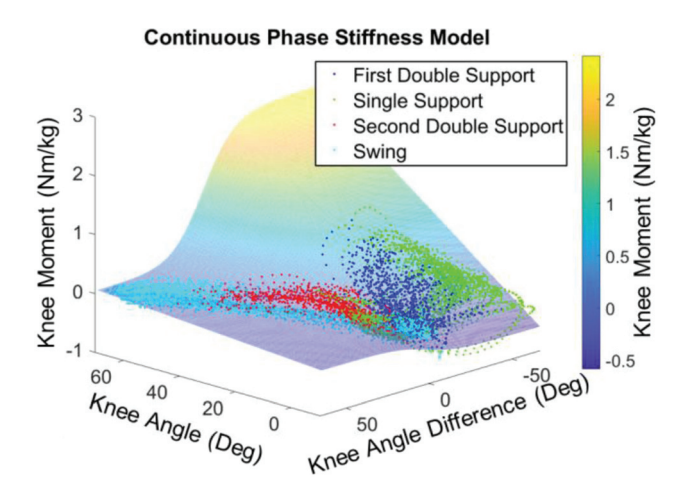


Fig. 8. Estimated biological torque (colored three-dimensional surface) by the continuous-phase stiffness model matches well with respect to the training dataset of 23 able-bodied subjects (colored dots indicate four phases of each gait cycle).

method is more suitable for self-selected and fast walking speeds than slow walking speeds.

The trained continuous-phase stiffness model and the corresponding training dataset are visualized in Fig. 8. Notably, the transition between stance- and swing-phase stiffness models is smooth, as intended by the continuous-stiffness design.

### D. Evaluation of the Continuous-Phase Stiffness Model

We tested the generalization of our model by training with data from 22 subjects and then testing it on a new subject (not from the training set) to evaluate the knee moment estimation. The estimated knee moment for this subject walking at three speeds is shown in Fig. 9. The rms errors (and percentage) of the torque tracking at slow speed, self-selected speed, and fast speed are 0.0583 N·m/kg (13.68%), 0.0585 N·m/kg (8.27%), and 0.0874 N·m/kg (8.40%), respectively. The results demonstrate that the estimated knee moments were close to the actual knee moments, and the generated moment profiles were continuous and smooth. The black dashed line in the right column of Fig. 9 depicts the value of the sigmoid function  $S(\theta_{k,r}, \theta_{k,l}) \in [01]$  in (11) across the entire gait cycle. It shows that the stiffness model is more inclined to the stance-phase model ( $S(\theta_{k,r}, \theta_{k,l}) = 0$ ) during the first double-support and single-support phases, whereas the swing-phase stiffness model has a higher weight during the second double support and swing phases  $(S(\theta_{k,r}, \theta_{k,l}) = 1)$ .

### VI. EXPERIMENTS

To characterize the knee exoskeleton and evaluate controller performance, we conducted both benchtop and human subject experiments. Benchtop experiments aimed to evaluate the performance of the robot and its controller. The experiment with eight able-bodied subjects aimed to evaluate the tracking performance of the torque controller during walking at different speeds and muscle activity responses to exoskeleton assistance. Our protocol was approved by the City University of New York Institutional Review Board (CCNY IRB, application no.

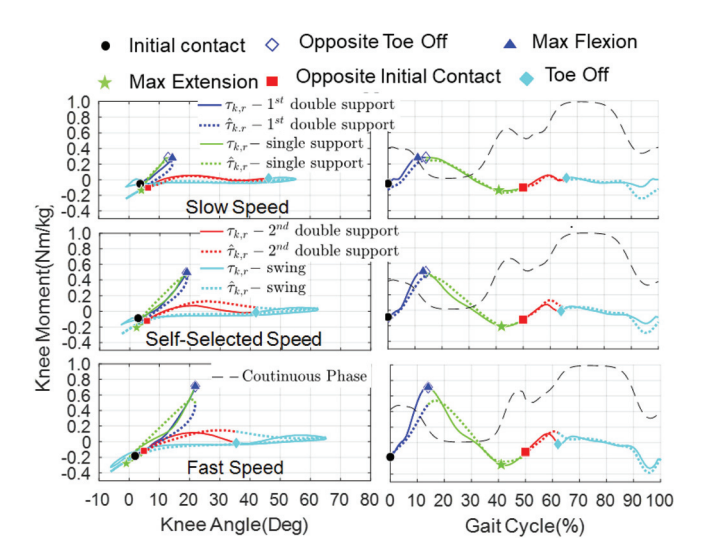


Fig. 9. Demonstration of the continuous-phase stiffness model (see Fig. 7) in one subject. The left column depicts the knee angle versus the estimated knee moment, and the right column depicts the gait cycle versus the estimated knee moment. The blue color indicates the single-support phase, the red color indicates the second double-support phase, and the cyan color indicates the swing phase. The solid line represents the biological knee moment, whereas the dashed line represents the estimated knee moment. The top, middle, and bottom rows show the slow, self-selected, and fast walking speed results, respectively. The black dashed line in the right column depicts the value of the sigmoid function  $S(\theta_{k,r},\theta_{k,l}) \in [01]$  in (11) across the entire gait cycle. It shows that the stiffness model is more inclined to the stance-phase model during the first double-support and single-support phases, whereas the swing-phase stiffness model has a higher weight during the second double-support and swing phases.

2018-0885) and NC State University (eIRB # 24675). Our study was performed in line with the CCNY IRB and NC State IRB Guidance.

### A. Benchtop Experiments

1) High-Backdrivability Demonstration: We conducted a dynamic backdrivability test to characterize backdrivability. The actuator's output shaft was manually rotated between  $-30^{\circ}$  and  $20^{\circ}$  at frequencies between 0.5 and 2 Hz. A loadcell measured the backdrive torque in unpowered mode, which was filtered (first-order, 1-Hz cutoff, low-pass Butterworth filter) to eliminate sensor noise. The measured rotation angle and backdrive torque are presented in Fig. 10. The results indicated that our exoskeleton exhibited a very low backdrive torque ( $\sim$ 0.22 N·m), indicating significantly better backdrivability than advanced SEA (8.5 N·m) [10] and other QDD-based exoskeletons (1.32 N·m) [29].

2) Stiffness Modulation With Torque Tracking Accuracy: The exoskeleton is required to provide both high-stiffness and low-stiffness control conditions as the human knee joint exhibits high stiffness in the stance phase and low stiffness in the swing phase. In this experiment, a constant stiffness was set and the output shaft was manually rotated, whereas the desired and actual torque were recorded. As shown in Fig. 11, we tested the torque tracking accuracy under low (1 N·m/rad), medium (100 N·m/rad), and high (350 N·m/rad) stiffness control conditions. The rms errors (and percentage of the desired peak torque) of the torque tracking were 0.08 N·m (8.06%), 0.31 N·m (5.24%),

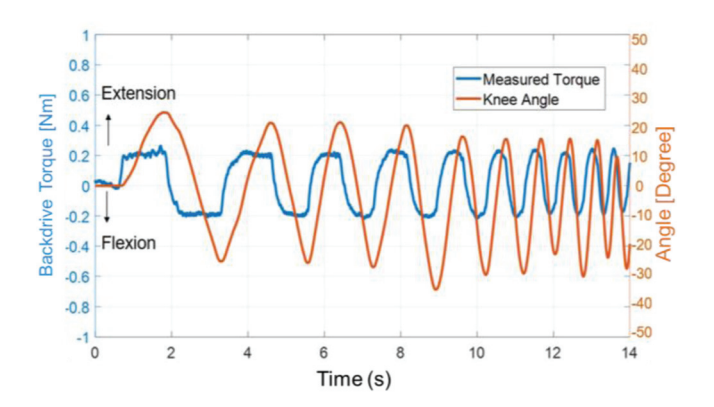


Fig. 10. Backdrivability test of the knee exoskeleton in unpowered condition. The maximum backdrive torque was approximately 0.22 N·m, which is less than state-of-the-art results of 8.5 N·m [10] (SEA actuator) and 1.32 N·m [29] (QDD actuator).

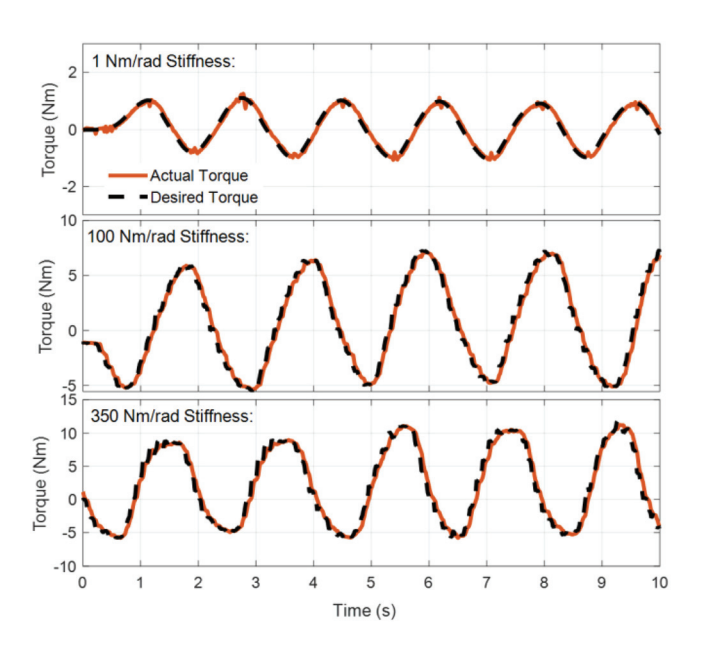


Fig. 11. Torque tracking performance under relatively low (1 N·m/rad), medium (100 N·m/rad), and high (350 N·m/rad) stiffness control conditions. The measured torque (orange) tracked well the desired torque (black dashed line). The rms errors (and percentage of the desired peak torque) of the torque tracking were 0.08 N·m (8.06%), 0.31 N·m (5.24%), and 0.64 N·m (0.987), respectively.

and  $0.64 \, \mathrm{N\cdot m} \, (5.36\%)$  at low, medium, and high stiffness control conditions, respectively. The tracking accuracy was superior to the stiffness control results (SEA actuators) reported in [10].

3) Exoskeleton Torque Control Bandwidth Evaluation: For the torque control bandwidth test, a chirp signal was used as the reference torque, whose magnitude was set to 5, 10, and 15 N·m. The Bode plot (see Fig. 12) showed that the bandwidths were 38.3, 39.3, and 40.7 Hz for chirp magnitudes of 5, 10, and 15 N·m, respectively. The control bandwidth satisfied the design specification, being much higher than the requirement for human walking. The high control bandwidth can be helpful in more dynamic human activities like running and balance control in response to unexpected external disturbances. Compared with the 5 Hz bandwidth of one advanced exoskeleton using SEA

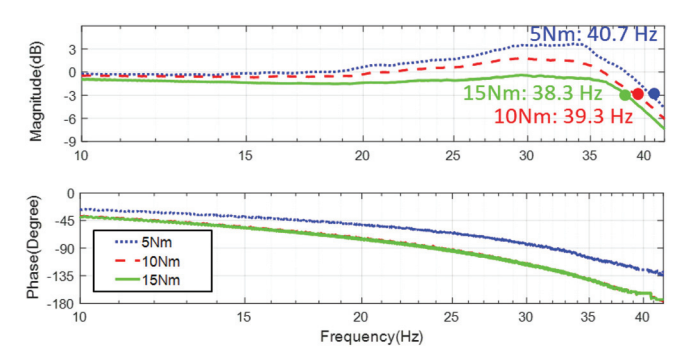


Fig. 12. Bode plot for torque control for reference torque with 5, 10, and 15 N·m chirp signals. The high bandwidth (highest value was 40.7 Hz) demonstrates the ability to handle more dynamic human movements in comparison with state-of-the-art results (5 Hz bandwidth in [10]).

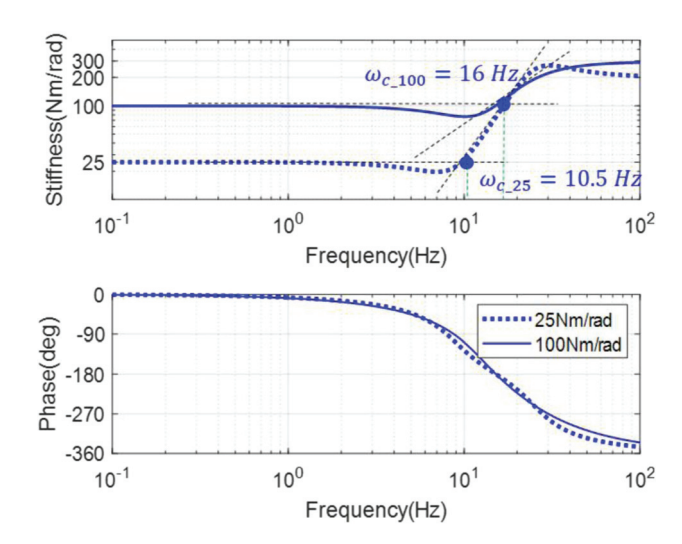


Fig. 13. Bode diagram of exoskeleton stiffness transfer function from the experiment. The input was a human knee angle  $\theta_h(t)$  with a 5°step function. The first corner frequency values showed the bandwidth of the stiffness control was 10.5 Hz for 25 N·m/rad reference stiffness and 16 Hz for 100 N·m/rad reference stiffness, which was higher than human lower-limb movement frequency and was able to track reference stiffness accurately with the exoskeleton.

[10], our exoskeleton had a higher control bandwidth, making it more robust to uncertainties.

4) Exoskeleton Stiffness Control Bandwidth Evaluation: To evaluate the stiffness control bandwidth in a benchtop test, we used step response with a 5° step function of human knee angle  $\theta_h(t)$  as the input. We collected data with two reference stiffness conditions (25 N·m/rad and 100 N·m/rad), and the frequency response of the actual stiffness transfer function, see (2), is analyzed in Fig. 13. We identified the transfer function containing two poles and two zeros by the function tfest of MATLAB R2019b for both reference stiffness conditions. The results are shown in Fig. 13. We found the first corner frequency was 10.5 Hz for 25 N·m/rad reference stiffness and 16 Hz for 100 N·m/rad reference stiffness. Since the frequency of the human lower-limb movement is typically less than 10.5 Hz, the stiffness control bandwidth demonstrated our proposed stiffness-based continuous torque controller was able to track reference stiffness accurately with the exoskeleton.

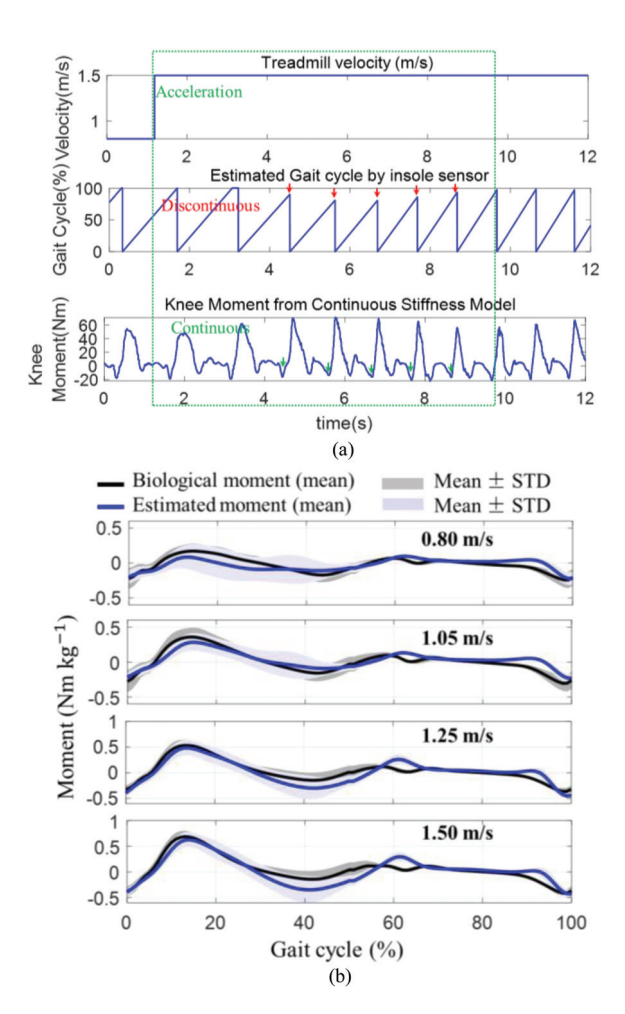


Fig. 14. (a) Comparison between the knee moment estimation based on the gait cycle and the proposed continuous torque controller (see Fig. 7). The proposed controller can adapt to walking speed from 0.8 to 1.5 m/s, and the estimated knee moment is continuous, in contrast to the discontinuous profile generated from the gait-cycle-based method. (b) Estimated moment versus the actual biological knee moment for four speeds (mean  $\pm$  std of eight subjects' data). We recorded 10 strides data for each subject/speed.

#### B. Human Subject Experiments

The objectives of the human experiments are the following:

- 1) to evaluate the movement synergy of our continuous torque controller with humans at different walking speeds;
- to evaluate the capability of the system to track the desired torque and show that our exoskeleton with the proposed controller does not cause a significant change in knee kinematics;
- 3) to understand the effect on lower-limb muscle activities.
- 1) Accurate Biological Torque Estimation With Our Stiffness Model: To illustrate the benefit of our proposed controller, the knee moment estimation from the continuous torque controller is shown in Fig. 14(a). As the treadmill velocity changed from 0.8 to 1.5 m/s, the gait cycle shrank, and our proposed method automatically adapted to the changing speed and generated a continuous knee moment because it only required the current knee joint angle to estimate the knee moment and thus did not explicitly rely on the gait phase estimation.

TABLE V
RMSE AND CORRELATION BETWEEN THE ESTIMATED MOMENT AND THE
BIOLOGICAL MOMENT FOR DIFFERENT SPEEDS

Speed (m/s)	0.80	1.05	1.25	1.50	Average
RMSE (Nm/kg)	0.079	0.077	0.073	0.086	0.079
Correlation	84.3%	90.3%	93.3%	92.9%	90.2%

TABLE VI RMSE AND CORRELATION BETWEEN THE ESTIMATED MOMENT AND THE BIOLOGICAL MOMENT UNDER 1.25 m/s WALKING SPEED

Subject	1	2	3	4	5
RMSE (Nm/kg)	0.087	0.069	0.079	0.083	0.061
Correlation	87.1%	95.0%	89.3%	88.7%	96.1%
Subject	6	7	8	Average	
RMSE (Nm/kg)	0.066	0.073	0.066 0.073±0		0.009
KWISE (NIII/Kg)	0.000	0.073	0.000	(mean ±	(SD)
Correlation	95.8%	95.3%	94.7%	93.3%	

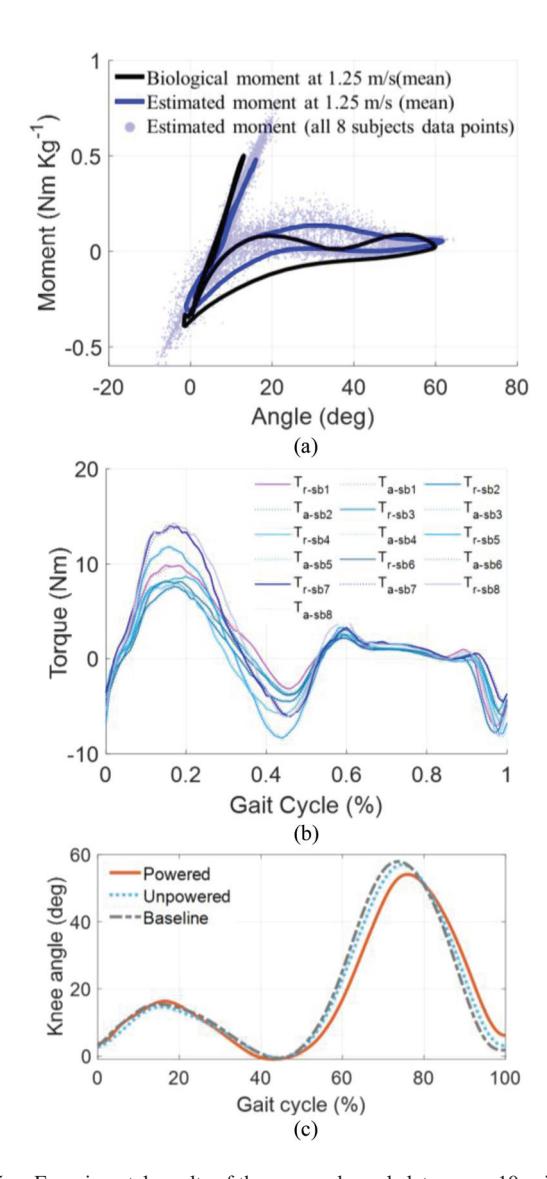
To evaluate the accuracy of the estimated biological knee moment by our stiffness model, we compared the estimated knee moment and the biological moment for eight subjects at four speeds (0.80 m/s, 1.05 m/s, 1.25 m/s, and 1.50 m/s). Fig. 14(b) shows the comparison results between the estimated moment and the actual biological knee moment for eight subjects. To analyze the prediction accuracy and correlation, we calculated the rms error and correlation percentage for different speeds (eight subjects). As shown in Table V, the group average rms error is 0.079 N·m/kg, and the group average correlation is 90.2%. The results demonstrate that the proposed stiffness model can estimate knee joint moment under all three speeds of walking. In particular, the estimated moment of 1.25 m/s walking speed (normal walking speed) has the best accuracy and correlation.

2) Performance of Stiffness-Based Continuous Torque Controller: This section evaluates the continuous torque control feature of the proposed controller. Fig. 15 shows the torque—angle behavior of our knee exoskeleton over 10 gait cycles collected from 8 subjects walking at 1.25 m/s on the treadmill.

In Fig. 15(a), the light blue dots represent the estimated moment–angle data points for the eight subjects, the blue line shows the averaged curve of normalized estimated knee moment and knee angle from the continuous-stiffness model of the eight subjects, and the black line shows the averaged curve of the normalized biological knee moment and the knee angle. We observed that the tendency of the two curves in Fig. 15(a) is similar, especially in the stance phase.

As shown in Table VI, the largest rms error (0.087 N·m/kg) between the estimated moment and the biological moment is found in subject 1, whereas subject 5's data have the smallest rms error (0.061 N·m/kg). The mean  $\pm$  SD for the group rms error is 0.073  $\pm$  0.009 N·m/kg. The largest correlation (96.1%) is found in subject 1, whereas subject 5's data have the smallest correlation (87.1%). The average correlation is 93.3%. These results indicate that the proposed joint moment estimation method can accurately estimate knee moment during walking at 1.25 m/s speed.

To evaluate the torque tracking performance of the stiffnessbased continuous control, the average torque reference and the average actual assistive torque from eight subjects are shown in



Experimental results of the powered exoskeleton over 10 gait cycles at 1.25 m/s treadmill walking with 30% biological torque assistance. (a) Knee angle versus joint moment from eight able-bodied subjects. The light blue dots show the eight subjects' data points that are the averaged curve of normalized estimated knee moment and knee angle, the blue line shows the averaged curve of normalized estimated knee moment and knee angle curve from the continuous-stiffness model, and the black line shows the averaged curve of the normalized biological knee moment and the knee angle. The torque profile generated by the stiffness-based continuous torque controller was similar to the biological knee joint moment. (b) Torque reference  $\tau_r$  and actual assistive torque  $au_a$  of eight subjects. The torque tracking rms error (and percentage) is 0.23 N·m (5.39%). It demonstrated that the controller was able to track the torque reference accurately. (c) Knee angle versus gait cycle averaged across eight subjects. Mean knee angle versus gait cycle averaged across eight subjects. It demonstrated that the kinematics did not significantly change between unpowered and baseline conditions (p < 0.001). The maximum knee flexion angle in the powered condition decreased about 2.8° relative to the baseline condition.

Fig. 15(b). The torque (percentage) rms error across the eight subjects is  $0.25~\text{N}\cdot\text{m}$  (5.40% of peak torque). The experimental results demonstrated the capability of the system to track the desired torque at corresponding joint angles using our controller. Another feature is that the controller does not cause a significant difference in knee kinematics (in terms of knee angles) between unpowered and baseline conditions across all eight subjects, as

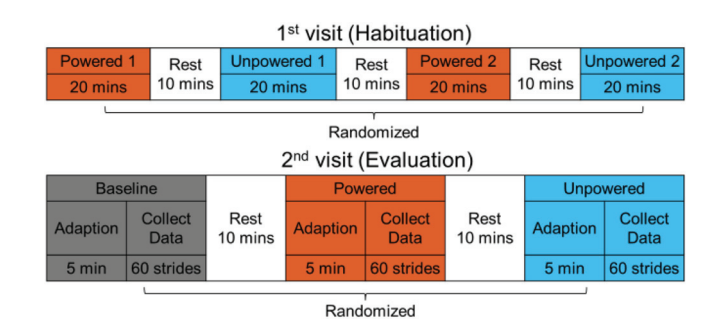


Fig. 16. Protocol of human testing included two visits for habituation and evaluation, respectively. The second visit was scheduled two days after the first visit so that the subject could have sufficient rest. In both the visits, the conditions were randomly alternated to reduce bias.

TABLE VII
EIGHT ABLE-BODIED SUBJECTS INFORMATION

Subject No.	Gender	Age	Height (m)	Weight (kg)
1	Male	31	1.76	70
2	Male	26	1.84	68
3	Male	27	1.74	75
4	Male	40	1.75	80
5	Female	29	1.74	70
6	Male	30	1.73	72
7	Male	29	1.81	100
8	Female	24	1.72	80

shown in Fig. 15(c) (prediction correlation coefficient =  $0.983 \pm 0.008$ , p < 0.001). The knee angle profile between the powered and baseline conditions was also similar (prediction correlation coefficient =  $0.936 \pm 0.047$ , p < 0.001), with only about a  $2.8^{\circ}$  decrease in the maximum flexion angle.

3) EMG Experimental Protocol: We designed and implemented a two-session protocol to evaluate the presented controller design (see Fig. 16). Session 1 was for a fitting, parameter tuning, and neuromuscular adaptation to the exoskeleton. A rest period of between 2 and 5 days occurred before session 2 to limit the effect of muscle fatigue. In visit 2, we collected experimental data. Following similar human evaluation studies [30], [48], [57], [62], eight able-bodied subjects (six males and two females, as shown in Table VII) with a mean age of 29.5 ( $\pm 4.8$ ) years, a mean height of 1.76 ( $\pm 0.04$ ) m, and mean weight of 76.1 ( $\pm 10.1$ ) kg were enrolled with approval from the Institutional Review Board.

In the first visit, we tuned and adjusted the exoskeleton to best fit the subject. The subject then walked with the exoskeleton on a treadmill at 1.25 m/s in two conditions (powered and unpowered) with a total of four walking bouts. Each walking bout lasted 20 min and was interspaced with 10-min rest periods. We randomized the order of conditions to minimize the learning effect. In the powered condition, the exoskeleton provided assistance torque equivalent to 30% of the biological torque at the knee. In the unpowered condition, the participant wore the exoskeleton while it was turned off and provided no active torque. An adaptation time of 40 min allowed the neuromuscular activity to adapt sufficiently to wearing the exoskeleton [14].

In session 2, the participant walked in three conditions (powered, unpowered, and baseline) while we recorded data. The

powered and unpowered conditions were the same as in session 1, and the baseline condition was walking without the exoskeleton. We randomized the order of the conditions to prevent the influence of order and reduce bias on the data collected. For each condition, the participant walked on the treadmill at 1.25 m/s for 5 min before data were collected over the next 60 strides. The participant rested for 10 min between two consecutive tests. Fig. 16 shows the detailed protocol of the two-visit study.

The collected data included gait phase, knee joint angles, exoskeleton torques (estimated and measured), and electromyography (EMG) measurements. We used footswitches (B&L Engineering, USA) worn inside the subject's shoes to identify ground contact times and then segmented all data into strides in postprocessing. Knee joint angles in the sagittal plane were calculated using four IMUs strapped to the thigh and shank segments on both legs of the subject. Eight wireless EMG sensors (Noraxon, Scottsdale, AZ, USA) recorded muscle activity of the eight muscles on the right leg of the subject at 2000 Hz: rectus femoris (RF), vastus lateralis (VL), vastus medialis (VM), biceps femoris (BF), semitendinosus (SEM), tibialis anterior (TA), lateral gastrocnemius (LG), and medial gastrocnemius (MG). EMG data were notch filtered with a band-stop filter (58-62 Hz, 4th-order, zero-phase Butterworth filter) and bandpass filtered (30–500 Hz, 4th-order, zero-phase Butterworth filter) and rectified. For each muscle, rms and peak values of the EMG signal were extracted for 10 strides, averaged, and then normalized to the rms or peak (respectively) in the baseline averaged condition. We normalized the rms and peak values across participants. For visualization, the time series data were filtered by a low-pass filter (20 Hz, 4th-order, zero-phase Butterworth filter), normalized to 1001 data points, and averaged across 10 strides.

4) EMG Results: To evaluate the performance of the exoskeleton assistance and the proposed controller, Fig. 17 depicts the normalized EMG of the eight muscles for one representative subject. The results showed that the peak EMG signal of the eight muscles in the unpowered condition was the highest compared with baseline and powered conditions, which was due to the extra weight and friction introduced by the exoskeleton. The peak EMG signal of ankle extensors and flexors (TA, LG, and MG) was the lowest in the baseline condition, suggesting that the knee exoskeleton (both powered and unpowered conditions) increased the muscle activity for ankle muscle groups.

RMS EMG and maximum EMG averaged across 10 gait cycles and 8 subjects under the three test conditions are shown in Fig. 18 and Table VIII . Paired t-tests with Bonferroni correction (p=0.0031) were used to determine if the reduction in the muscle activity between powered and unpowered conditions and between powered and baseline conditions was statistically significant. Changes in peak and rms muscle activity are reported in Table VIII and Fig. 18. Muscle activities of all eight muscles were highest in the unpowered condition.

# VII. DISCUSSION AND CONCLUSION

The overarching goal of this work was to understand the benefits of a high-performance knee exoskeleton through stiffness

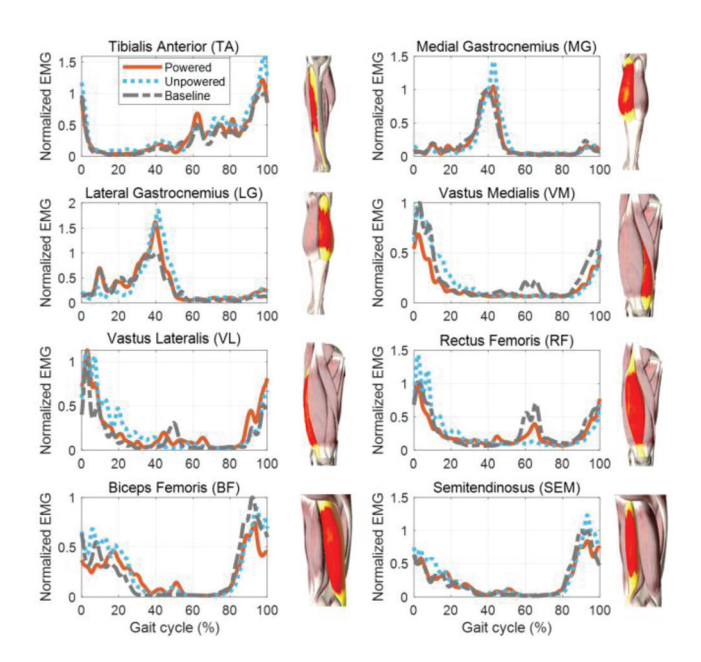


Fig. 17. Normalized (baseline maximum = 1) EMG versus gait cycle for eight muscles (TA, MG, LG, VM, VL, RF, BF, and SEM) of a single subject. The blue dotted, gray dashed, and orange solid lines represent the time-normalized ensemble averages across all gait cycles in baseline, unpowered, and powered conditions, respectively.

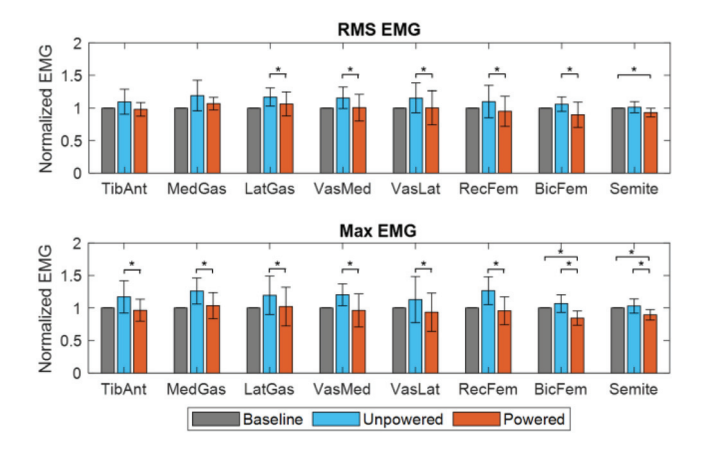


Fig. 18. Normalized rms and maximum EMG averaged across 10 gait cycles and multiple subjects under three conditions (baseline, unpowered, and powered) for TA (n=7), MG (n=4), LG (n=7), VM (n=8), VL (n=7), RF (n=6), BF (n=7), and SEM (n=7), where n is the number of subjects whose EMG data were used for analysis of each muscle. The EMG signal of some muscles of some subjects was discarded due to signal artifacts. Asterisks indicate that the reduction in muscle activity between powered and unpowered conditions and between powered and baseline conditions was statistically significant (paired t-test with Bonferroni correction, p=0.0031). Compared with the unpowered condition, the powered result showed an overall rms EMG reduction of 8.60%–15.22% and a maximum EMG reduction of 12.36%–24.89%. The error bars represent  $\pm 1$  standard deviation.

modeling and advanced control methods for continuous torque assistance during overground walking. The proposed design and control methods result in a lightweight and compliant portable exoskeleton with a high bandwidth of stiffness control and high torque tracking accuracy. The results of this research are significant because of the following reasons.

_	_		_		_		
	Unpo	Powered vs Unpowered (Powered - 1)%		wered vs seline $\frac{\operatorname{red}}{\operatorname{ne}} - 1$ %	Powered vs Baseline $\left(\frac{\text{Powered}}{\text{Baseline}} - 1\right)\%$		
	RMS	Maximum	RMS	Maximum	RMS	Maximum	
TA	-8.60%	-16.04%	9.55%	17.07%	-1.92%	-3.52%	
BF	-15.22%	-20.49%	6.04%	6.76%	-10.24%	-15.68%	
SEM	-7.45%	-12.36%	1.44%	3.01%	-6.85%	-10.58%	
MG	-8.97%	-17.94%	19.11%	26.08%	6.88%	3.55%	
LG	-9.34%	-14.61%	16.89%	19.50%	6.44%	2.18%	
VM	-12.99%	-19.64%	15.63%	20.29%	0.72%	-3.73%	
VL	-13.52%	-16.38%	15.45%	12.88%	0.32%	-6.67%	
RF	-13 68%	-24 89%	9 91%	26.65%	-4 95%	-4 39%	

TABLE VIII

COMPARISON OF THE RMS AND MAX EMG AMONG DIFFERENT
CONDITIONS—EIGHT-SUBJECT GROUP RESULTS

- It derives both modeling and continuous torque control for QDD exoskeletons. Presented theory and simulation delineate the advantages of QDD actuation in comparison with the SEA actuation method.
- 2) It proposes a stiffness-based continuous torque controller that estimates the biological torque in real-time and is adaptable to different overground walking speeds.
- It comprehensively evaluates and demonstrates the feasibility of a portable knee exoskeleton to reduce muscular activities during level-ground walking in able-bodied individuals.

# A. Advantages of Stiffness Modeling and Stiffness-Based Continuous Torque Control

Leveraging the analytical stiffness model, theoretical and experimental benchmark results demonstrate that the QDD actuator outperforms SEA in terms of both torque control and stiffness control. We showed that our QDD actuator has a large stiffness bandwidth that covers the frequency of normal human walking and running. It also achieved a small torque tracking error under a wide range of stiffnesses.

We also proposed a control framework to generate a stiffness-based continuous torque assistance profile while ensuring a smooth transition during speed changes. Previous studies [26], [33] involving stiffness models were not able to adapt to speed changes and would generate a discontinuous torque profile. Since they depend on gait phase estimations, the sudden jump will appear at these points.

#### B. Neuromuscular Response and Interpretations

We investigated the effect of a portable high-performance knee exoskeleton on able-bodied subjects during level-ground walking. Previous studies demonstrated that it is possible to reduce muscle activities with a portable knee exoskeleton or exosuit. However, such benefits have only been shown in more torque-demanding conditions, e.g., incline/decline walking [20], [30], or in particular, preswing and swing gait phases for inflatable exosuit pressure control [26]. This work comprehensively

evaluates the effects of a portable knee exoskeleton on ablebodied subjects for level-ground walking. The results suggest that a powered lightweight portable knee exoskeleton has the potential to reduce several lower-limb muscle activations for level-ground walking.

Compared with the unpowered condition, the rms and maximum EMG of all eight muscles decreased in the powered condition. This reduction is remarkable in terms of rms EMG for all three knee extensors examined (VM, VL, and RF) and two knee flexors (LG and BF) and for all eight muscles in terms of maximum EMG (see Fig. 18 and Table VIII). This result illustrates that our controller can effectively assist level-ground walking when compared with the unpowered case. Further improvement may be possible by separately optimizing the assistance profile in the stance and swing phases.

Interestingly, although the torque assistance is applied to the knee joint, a reduction in peak ankle extensor (TA) muscle activation is also observed. This agrees with the findings reported in [15], [48], and [49] that altering the dynamics of the assisted joint may affect the dynamics of other joints. Therefore, although the knee joint primarily dissipates energy during the gait cycle [63], benefits to the overall level-ground walking performance may still be possible thanks to a corresponding reduction in muscle activity at other joints.

The reduction in muscle activation between powered exoskeleton and baseline is lower than that between powered and unpowered, with two muscles (SEM and BF) showing significant differences in peak EMG across the entire gait cycle. The two main factors limiting the reduction in muscle activity between baseline and powered conditions were device weight and standardized assistance profiles. Although we optimized the design of our exoskeleton to be lightweight (3.5 kg bilateral weight) and compliant (0.22 N·m backdrive torque), the increase in muscle activity between baseline and unpowered demonstrates that mass and/or friction had an effect. The torque assistance essentially mitigates the impact of mass/friction, but the benefit does not yet substantially exceed the imposed mass penalty. Further improvement of hardware design might alleviate the impact of mass on muscle activity during walking. Second, the torque assistance profile is based on a pretrained population-averaged dataset and is not tailored to each participant. Individualized torque assistance profiles could provide a further reduction in muscle activity between powered and baseline conditions. We discuss this limitation in the following section.

### C. Limitations of the Study

Here, we note some limitations of our study. First, we chose an assistive torque that mimics biological torque. Although it is an intuitive control approach in wearable robotics, some literature reports that the optimal exoskeleton torque profile for human performance augmentation may not be proportional to the biological torque [56]. Determining the optimal exoskeleton torque profile is challenging as the human—exoskeleton interaction must be fully understood, including how assistive torque impacts the dynamics of human muscles. Nonetheless, a proportional biological torque profile was worth investigating since it is

Parameter	Unit	Conventional Actuator	SEA	QDD
Motor	-	Maxon EC flat 45 651618 [20]	Kollmorgen T-2950 [19]	Ours
Nominal voltage	V	24	38.4	42
Nominal current	A	3.29	1	7.5
Nominal Torque	Nm	0.134	0.813	2.165
Motor resistance	Ω	0.573	19.2	0.58
Motor inductance	mH	0.301	41	0.21
Motor friction coefficient	Nm·s/rad	0.01	0.034	0.08
Torque constant	Nm/A	0.0404	0.813	0.2886
Motor inertia	g·cm <sup>2</sup>	181	3932	895
Gear ratio	-	113:1	100:1	6:1
Transmission stiffness	Nm /rad	500	200	500

TABLE IX
PARAMETERS IN THE HUMAN–EXOSKELETON COUPLED MODEL

unlikely to have a negative impact on human performance and is viable and simple for assisting wearers.

A second limitation is the misalignment of the exoskeleton and the human knee joint. Although this is a common issue for a rigid powered exoskeleton, the misalignment may induce an undesired interaction force that affects the comfortable operation of the exoskeleton [64]. Our previous work [55] developed a novel mechanism that used a rolling knee joint and double-hinge structure to reduce 74% of the joint misalignment at maximum knee flexion. However, due to the complexity of the mechanical structure, our previous design increases the total weight of the exoskeleton. It thus induces an undesired mass penalty to the overall human performance. Another approach to solving this problem is to use a jointless actuator design that eliminates the need for joint alignment in the first place. An example is the soft inflatable pneumatic knee exosuit developed by Sridar et al. [26]. Although the exosuit does not have joint alignment issues thanks to its soft nature, its actuator is powered by an external pneumatic source. Thus, the tethered pneumatic design limits its portability and bandwidth.

### D. Conclusion and Future Work

In this work, a continuous-phase stiffness model and the corresponding stiffness-based continuous torque controller are proposed and evaluated on a portable knee exoskeleton with eight able-bodied subjects during treadmill walking. This stiffness model can achieve a large and sufficient stiffness bandwidth (16 Hz) to cover the normal human walking frequency range, and the controller achieves a small torque tracking error (0.23 N·m) under different stiffness. Our continuous torque controller requires no gait phase estimation and can adapt to varying speeds and generate a continuous torque profile. Reducing the muscle activity of able-bodied subjects for level-ground walking using a portable knee exoskeleton has traditionally been considered a difficult task [65]. However, by leveraging our lightweight portable knee exoskeleton and our proposed continuous stiffness-based torque controller, our neuromuscular walking experiments demonstrate that both the rms and maximum EMG of all eight muscles decreased (remarkable for three extensors and two flexors) in the powered condition relative to the unpowered condition and two out of eight lower extremity muscles have a significant reduction in muscle activation in the powered condition relative to the baseline (no-exoskeleton) condition. Compared with the result of the baseline condition in Table VIII, the results showed that the powered exoskeleton could reduce the maximum EMG of knee extensors (VM, VL, and RF), knee flexors (BF and SEM), and ankle muscle (TA) and reduce the rms of knee extensor (RF), knee flexors (BF and SEM), and ankle muscle (TA). But the rms and maximum EMG of the ankle plantar flexors (MG and LG) were increased by 3.55% and 2.18%, respectively. Therefore, it can be concluded that the knee exoskeleton can reduce the EMG signal of the knee flexor and extensor muscles. In contrast, the weight of the exoskeleton might cause a slight increase in the EMG signal of the ankle plantar flexors, and it cannot be mitigated by knee joint torque assistance.

A recent study [49] demonstrated that a portable knee exoskeleton could only improve mobility for stroke subjects with a moderate level of neurological impairments because the device was too heavy and stiff. Since our knee exoskeleton is more lightweight and compliant (3.5 kg versus 5.4 kg Keeogo), we will study whether the robot and associated stiffness-based continuous torque controller can benefit broader populations with mild, moderate, and severe levels of neurological impairments.

It may be worthwhile in future work to use an assistive torque profile other than the proportional biological torque profile or optimize the torque profile using human-in-the-loop methods [56], [66]. In addition, the adaptability of the controller to different terrains, such as incline/decline walking and stair climbing, will be thoroughly studied and evaluated. We are investigating the quasi-stiffness profiles during level-ground walking, incline walking [14], and loaded walking [38]. In future work, we will investigate the hypothesis that the continuous-stiffness model (two modes) from this work can be generalized to multiple stiffness modes to produce assistive torque for different terrain conditions.

### APPENDIX

See table IX

#### ACKNOWLEDGMENT

Any opinions, findings, and conclusions or recommendations expressed in this material are those of the author (s) and do not necessarily reflect the views of the funding organizations.

#### REFERENCES

[1] A. J. Young and D. P. Ferris, "State of the art and future directions for lower limb robotic exoskeletons," *IEEE Trans. Neural Syst. Rehabil. Eng.*, vol. 25, no. 2, pp. 171–182, Feb. 2017.

- [2] G. S. Sawicki, O. N. Beck, I. Kang, and A. J. Young, "The exoskeleton expansion: Improving walking and running economy," *J. NeuroEng. Rehabil.*, vol. 17, no. 1, pp. 1–9, 2020.
- [3] M. B. Yandell, B. T. Quinlivan, D. Popov, C. Walsh, and K. E. Zelik, "Physical interface dynamics alter how robotic exosuits augment human movement: Implications for optimizing wearable assistive devices," *J. Neuroeng. Rehabil.*, vol. 14, no. 1, 2017, Art. no. 40.
- [4] K. E. Gordon and D. P. Ferris, "Learning to walk with a robotic ankle exoskeleton," J. Biomech., vol. 40, no. 12, pp. 2636–2644, 2007.
- [5] L. M. Mooney, E. J. Rouse, and H. M. Herr, "Autonomous exoskeleton reduces metabolic cost of human walking during load carriage," *J. Neuroeng. Rehabil.*, vol. 11, no. 1, pp. 1–11, 2014.
- [6] M. B. Wiggin, G. S. Sawicki, and S. H. Collins, "An exoskeleton using controlled energy storage and release to aid ankle propulsion," in *Proc. IEEE Int. Conf. Rehabil. Robot.*, 2011, pp. 1–5.
- [7] S. Collins, M. B. Wiggin, and G. Sawicki, "An exoskeleton that uses no energy yet reduces the metabolic cost of human walking," *Nature*, vol. 522, pp. 212–215, 2015.
- [8] A. T. Asbeck, K. Schmidt, and C. J. Walsh, "Soft exosuit for hip assistance," Robot. Auton. Syst., vol. 73, pp. 102–110, 2015.
- [9] J. Lee, H. R. Warren, V. Agarwal, M. E. Huber, and N. Hogan, "Modulating hip stiffness with a robotic exoskeleton immediately changes gait," in *Proc. IEEE Int. Conf. Robot. Automat.*, 2020, pp. 733–739.
- [10] I. Kang, H. Hsu, and A. Young, "The effect of hip assistance levels on human energetic cost using robotic hip exoskeletons," *IEEE Robot. Automat. Lett.*, vol. 4, no. 2, pp. 430–437, Apr. 2019.
- [11] D. Pinto-Fernandez et al., "Performance evaluation of lower limb exoskeletons: A systematic review," *IEEE Trans. Neural Syst. Rehabil. Eng.*, vol. 28, no. 7, pp. 1573–1583, Jul. 2020.
- [12] Y. K. Cho, K. Kim, S. Ma, and J. Ueda, "A robotic wearable exoskeleton for construction worker's safety and health," in *Proc. ASCE Construction Res. Congr.*, 2018, pp. 19–28.
- [13] E. Tricomi et al., "Underactuated soft hip exosuit based on adaptive oscillators to assist human locomotion," *IEEE Robot. Automat. Lett.*, vol. 7, no. 2, pp. 936–943, Apr. 2022.
- [14] M. K. MacLean and D. P. Ferris, "Energetics of walking with a robotic knee exoskeleton," J. Appl. Biomech., vol. 35, no. 5, pp. 320–326, 2019.
- [15] K. Shamaei, M. Cenciarini, A. A. Adams, K. N. Gregorczyk, J. M. Schiffman, and A. M. Dollar, "Biomechanical effects of stiffness in parallel with the knee joint during walking," *IEEE Trans. Biomed. Eng.*, vol. 62, no. 10, pp. 2389–2401, Oct. 2015.
- [16] G. S. Sawicki, C. L. Lewis, and D. P. Ferris, "It pays to have a spring in your step," *Exercise Sport Sci. Rev.*, vol. 37, no. 3, pp. 130–138, 2009.
- [17] X. Yang et al., "Spine-inspired continuum soft exoskeleton for stoop lifting assistance," *IEEE Robot. Automat. Lett.*, vol. 4, no. 4, pp. 4547–4554, Oct. 2019.
- [18] E. J. Park et al., "A hinge-free, non-restrictive, lightweight tethered exosuit for knee extension assistance during walking," *IEEE Trans. Med. Robot. Bionics*, vol. 2, no. 2, pp. 165–175, May 2020.
- [19] N. Karavas, A. Ajoudani, N. Tsagarakis, J. Saglia, A. Bicchi, and D. Caldwell, "Tele-impedance based assistive control for a compliant knee exoskeleton," *Robot. Auton. Syst.*, vol. 73, pp. 78–90, 2015.
- [20] D. Lee, E. C. Kwak, B. J. McLain, I. Kang, and A. J. Young, "Effects of assistance during early stance phase using a robotic knee orthosis on energetics, muscle activity, and joint mechanics during incline and decline walking," *IEEE Trans. Neural Syst. Rehabil. Eng.*, vol. 28, no. 4, pp. 914–923, Apr. 2020.
- [21] G. Aguirre-Ollinger and H. Yu, "Lower-limb exoskeleton with variable-structure series elastic actuators: Phase-synchronized force control for gait asymmetry correction," *IEEE Trans. Robot.*, vol. 37, no. 3, pp. 763–779, Jun. 2021.
- [22] D. J. Braun, V. Chalvet, T.-H. Chong, S. S. Apte, and N. Hogan, "Variable stiffness spring actuators for low-energy-cost human augmentation," *IEEE Trans. Robot.*, vol. 35, no. 6, pp. 1435–1449, Dec. 2019.
- [23] S. Yu et al., "Quasi-direct drive actuation for a lightweight hip exoskeleton with high backdrivability and high bandwidth," *IEEE/ASME Trans. Mechatronics*, vol. 25, no. 4, pp. 1794–1802, Aug. 2020.
- [24] S. Yu et al., "Design and control of a high-torque and highly backdrivable hybrid soft exoskeleton for knee injury prevention during squatting," *IEEE Robot. Automat. Lett.*, vol. 4, no. 4, pp. 4579–4586, Oct. 2019.
- [25] D. Maeda et al., "Muscle synergy analysis of human adaptation to a variable-stiffness exoskeleton: Human walk with a knee exoskeleton with pneumatic artificial muscles," in Proc. 12th IEEE-RAS Int. Conf. Humanoid Robots, 2012, pp. 638–644.
- [26] S. Sridar et al., "Evaluating immediate benefits of assisting knee extension with a soft inflatable exosuit," *IEEE Trans. Med. Robot. Bionics*, vol. 2, no. 2, pp. 216–225, May 2020.

- [27] P. M. Wensing, A. Wang, S. Seok, D. Otten, J. Lang, and S. Kim, "Proprioceptive actuator design in the MIT cheetah: Impact mitigation and high-bandwidth physical interaction for dynamic legged robots," *IEEE Trans. Robot.*, vol. 33, no. 3, pp. 509–522, Jun. 2017.
- [28] B. Katz, J. Di Carlo, and S. Kim, "Mini cheetah: A platform for pushing the limits of dynamic quadruped control," in *Proc. Int. Conf. Robot. Automat.*, 2019, pp. 6295–6301.
- [29] H. Zhu, C. Nesler, N. Divekar, M. T. Ahmad, and R. D. Gregg, "Design and validation of a partial-assist knee orthosis with compact, backdrivable actuation," in *Proc. IEEE 16th Int. Conf. Rehabil. Robot.*, 2019, pp. 917–924.
- [30] D. Lee, B. J. Mclain, I. Kang, and A. Young, "Biomechanical comparison of assistance strategies using a bilateral robotic knee exoskeleton," *IEEE Trans. Biomed. Eng.*, vol. 68, no. 9, pp. 2870–2879, Sep. 2021.
- Trans. Biomed. Eng., vol. 68, no. 9, pp. 2870–2879, Sep. 2021.

  [31] H. Prasanth et al., "Wearable sensor-based real-time gait detection: A systematic review," Sensors, vol. 21, no. 8, 2021, Art. no. 2727.
- [32] D. A. Winter, Biomechanics and Motor Control of Human Gait: Normal, Elderly and Pathological. Waterloo, ON, Canada: Waterloo Biomechanics, 1991.
- [33] J. M. Caputo and S. H. Collins, "A universal ankle–foot prosthesis emulator for human locomotion experiments," *J. Biomech. Eng.*, vol. 136, no. 3, 2014, Art. no. 035002.
- [34] A. Martinez, B. Lawson, and M. Goldfarb, "A controller for guiding leg movement during overground walking with a lower limb exoskeleton," *IEEE Trans. Robot.*, vol. 34, no. 1, pp. 183–193, Feb. 2018.
- [35] B. Lim et al., "Delayed output feedback control for gait assistance with a robotic hip exoskeleton," *IEEE Trans. Robot.*, vol. 35, no. 4, pp. 1055–1062, Aug. 2019.
- [36] D. Quintero, D. J. Villarreal, D. J. Lambert, S. Kapp, and R. D. Gregg, "Continuous-phase control of a powered knee–ankle prosthesis: Amputee experiments across speeds and inclines," *IEEE Trans. Robot.*, vol. 34, no. 3, pp. 686–701, Jun. 2018.
- [37] N. Thatte, T. Shah, and H. Geyer, "Robust and adaptive lower limb prosthesis stance control via extended Kalman filter-based gait phase estimation," *IEEE Robot. Automat. Lett.*, vol. 4, no. 4, pp. 3129–3136, Oct. 2019.
- [38] K. G. Holt, R. C. Wagenaar, M. E. LaFiandra, M. Kubo, and J. P. Obusek, "Increased musculoskeletal stiffness during load carriage at increasing walking speeds maintains constant vertical excursion of the body center of mass," *J. Biomech.*, vol. 36, no. 4, pp. 465–471, 2003.
- [39] J. Zhang and S. H. Collins, "The passive series stiffness that optimizes torque tracking for a lower-limb exoskeleton in human walking," *Front. Neurorobot.*, vol. 11, 2017, Art. no. 68.
- [40] J. Chen, D. L. Damiano, Z. F. Lerner, and T. C. Bulea, "Validating model-based prediction of biological knee moment during walking with an exoskeleton in crouch gait: Potential application for exoskeleton control," in *Proc. IEEE 16th Int. Conf. Rehabil. Robot.*, 2019, pp. 778–783.
- [41] L. Liu, S. Leonhardt, C. Ngo, and B. J. Misgeld, "Impedance-controlled variable stiffness actuator for lower limb robot applications," *IEEE Trans. Automat. Sci. Eng.*, vol. 17, no. 2, pp. 991–1004, Apr. 2020.
- [42] K. Shamaei, G. S. Sawicki, and A. M. Dollar, "Estimation of quasi-stiffness of the human knee in the stance phase of walking," *PLoS One*, vol. 8, no. 3, 2013, Art. no. e59993.
- [43] C. A. Fukuchi, R. K. Fukuchi, and M. Duarte, "A public dataset of overground and treadmill walking kinematics and kinetics in healthy individuals," *PeerJ*, vol. 6, 2018, Art. no. e4640.
  [44] D. J. Farris and G. S. Sawicki, "The mechanics and energetics of human
- [44] D. J. Farris and G. S. Sawicki, "The mechanics and energetics of human walking and running: A joint level perspective," *J. Roy. Soc. Interface*, vol. 9, no. 66, pp. 110–118, 2012.
- [45] R. Jacobs, M. F. Bobbert, and G. J. van I. Schenau, "Mechanical output from individual muscles during explosive leg extensions: The role of biarticular muscles," *J. Biomech.*, vol. 29, no. 4, pp. 513–523, 1996.
- [46] G. J. van I. Schenau, M. Bobbert, and R. Rozendal, "The unique action of bi-articular muscles in complex movements," *J. Anatomy*, vol. 155, pp. 1–5, 1987.
- [47] G. J. van I. Schenau, "From rotation to translation: Constraints on multijoint movements and the unique action of bi-articular muscles," *Hum. Movement Sci.*, vol. 8, no. 4, pp. 301–337, 1989.
- [48] J. Kim et al., "Reducing the metabolic rate of walking and running with a versatile, portable exosuit," *Science*, vol. 365, no. 6454, pp. 668–672, 2019.
- [49] L. M. Mooney and H. M. Herr, "Biomechanical walking mechanisms underlying the metabolic reduction caused by an autonomous exoskeleton," J. Neuroeng. Rehabil., vol. 13, no. 1, pp. 1–12, 2016.
- [50] K. E. Zelik, K. Z. Takahashi, and G. S. Sawicki, "Six degree-of-freedom analysis of hip, knee, ankle and foot provides updated understanding of biomechanical work during human walking," *J. Exp. Biol.*, vol. 218, no. 6, pp. 876–886, 2015.

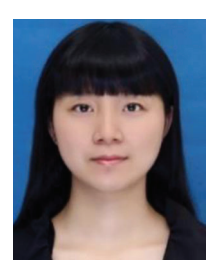
- [51] M. A. Ergin and V. Patoglu, "A self-adjusting knee exoskeleton for robotassisted treatment of knee injuries," in *Proc. IEEE/RSJ Int. Conf. Intell. Robots Syst.*, 2011, pp. 4917–4922.
- [52] Z. F. Lerner, D. L. Damiano, H.-S. Park, A. J. Gravunder, and T. C. Bulea, "A robotic exoskeleton for treatment of crouch gait in children with cerebral palsy: Design and initial application," *IEEE Trans. Neural Syst. Rehabil. Eng.*, vol. 25, no. 6, pp. 650–659, Jun. 2016.
- [53] C. A. McGibbon et al., "Evaluation of the Keeogo exoskeleton for assisting ambulatory activities in people with multiple sclerosis: An open-label, randomized, cross-over trial," J. Neuroeng. Rehabil., vol. 15, no. 1, 2018, Art. no. 117.
- [54] J. C. Mcleod, S. J. Ward, and A. L. Hicks, "Evaluation of the Keeogo<sup>TM</sup> dermoskeleton," *Disability Rehabil.*, Assistive Technol., vol. 14, no. 5, pp. 503–512, 2019.
- [55] K. Tamai, H. Kawamoto, and Y. Sankai, "Weight-supported walking assist device for knee osteoarthritis patients," in *Proc. IEEE 16th Int. Conf. Rehabil. Robot.*, 2019, pp. 374–379.
- [56] Y. Ding, M. Kim, S. Kuindersma, and C. J. Walsh, "Human-in-the-loop optimization of hip assistance with a soft exosuit during walking," *Sci. Robot.*, vol. 3, no. 15, 2018, Art. no. eaar5438.
- [57] P. W. Franks, G. M. Bryan, R. M. Martin, R. Reyes, and S. H. Collins, "Comparing optimized exoskeleton assistance of the hip, knee, and ankle in single and multi-joint configurations," *Wearable Technol.*, vol. 2, 2021, Art. no. e16.
- [58] J. Wang et al., "Comfort-centered design of a lightweight and back-drivable knee exoskeleton," *IEEE Robot. Automat. Lett.*, vol. 3, no. 4, pp. 4265–4272, Oct. 2018.
- [59] Y. Lee et al., "A flexible exoskeleton for hip assistance," in Proc. IEEE/RSJ Int. Conf. Intell. Robots Syst., 2017, pp. 1058–1063.
- [60] T. Zhang and H. Huang, "A lower-back robotic exoskeleton: Industrial handling augmentation used to provide spinal support," *IEEE Robot. Automat. Mag.*, vol. 25, no. 2, pp. 95–106, Jun. 2018.
- [61] W. Huo, S. Mohammed, Y. Amirat, and K. Kong, "Fast gait mode detection and assistive torque control of an exoskeletal robotic orthosis for walking assistance," *IEEE Trans. Robot.*, vol. 34, no. 4, pp. 1035–1052, Aug. 2018.
- [62] H. Zhu, C. Nesler, N. Divekar, V. Peddinti, and R. Gregg, "Design principles for compact, backdrivable actuation in partial-assist powered knee orthoses," *IEEE/ASME Trans. Mechatronics*, vol. 26, no. 6, pp. 3104–3115, Dec. 2021
- [63] A. M. Dollar and H. Herr, "Lower extremity exoskeletons and active orthoses: Challenges and state-of-the-art," *IEEE Trans. Robot.*, vol. 24, no. 1, pp. 144–158, Feb. 2008.
- [64] D. Zanotto, Y. Akiyama, P. Stegall, and S. K. Agrawal, "Knee joint misalignment in exoskeletons for the lower extremities: Effects on user's gait," *IEEE Trans. Robot.*, vol. 31, no. 4, pp. 978–987, Aug. 2015.
- [65] J. S. Lora-Millán, J. C. Moreno, and E. Rocon, "Assessment of gait symmetry, torque interaction and muscular response due to the unilateral assistance provided by an active knee orthosis in healthy subjects," in *Proc.* 8th IEEE RAS/EMBS Int. Conf. Biomed. Robot. Biomechatronics, 2020, pp. 229–234.
- [66] J. Zhang et al., "Human-in-the-loop optimization of exoskeleton assistance during walking," Science, vol. 356, no. 6344, pp. 1280–1284, 2017.



**Tzu-Hao Huang** Huang received the B.S. degree in occupational therapy from National Cheng Kung University, Tainan, Taiwan, in 2004, the M.S. degree in the Institute of Rehabilitation Science and Technology from National Yang Ming University, Taipei, Taiwan, in 2006, and the Ph.D. degree in mechanical engineering from National Taiwan University, Taipei, Taiwan, in 2013.

He is currently an Assistant Professor in the Department of Mechanical Engineering at the City College of New York. His major research area is control

and design of the rehabilitation and assistive devices, human-machine interface for assistive and rehabilitation device, brain-machine interface for subjects with movement disability, and the smart textile for physiological sensing in firefight, sport, and medical application.



Sainan Zhang received B.S. degree in automation from Xi'an University of Posts and Telecommunications, in 2015, the M.S. degree in control science of engineering from the University of Electronic Science and Technology of China, Sichuan, China, in 2018.

She is currently working towards the Ph.D. degree in the field of wearable robot supervised by Dr. Hao Su at the Department of Mechanical Engineering at the City University of New York, New York, USA. She is also a visiting scholar in the Department of Mechanical and Aerospace Engineering at the North

Carolina State University. Her current research interests include the control and optimization of lower-limb wearable robots.



wearable robots.

**Shuangyue Yu** received the B.S. degree in automation and the M.S. degree in control science of engineering from the Beijing University of Technology, Beijing, China, in 2014.

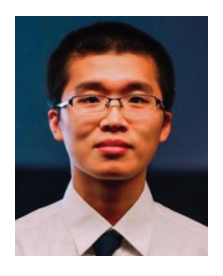
He is currently working towards the Ph.D. degree in wearable robot supervised by Dr. Hao Su with the Department of Mechanical Engineering, City University of New York, New York, NY, USA. He is also a Visiting Scholar with the Department of Mechanical and Aerospace Engineering, North Carolina State University. His research focuses on lower limb



Mhairi K. MacLean received the M.Eng. degree in biomedical engineering from the University of Glasgow, Glasgow, U.K., in 2014, the M.S. degree in kinesiology from the University of Michigan, Ann Arbor, MI, USA, in 2018, and the Ph.D. degree in biomedical engineering from the University of Florida, Gainesville, FL, USA, in 2020.

She was a Postdoctoral Researcher with Hao Su's Laboratory, City University of New York. She is currently an Assistant Professor with the Department of Mechanical Engineering, University of Twente,

Enschede, The Netherlands. Her current research interests include wearable 1285 robots and human biomechanics.



Junxi Zhu received the B.S. from Shanghai Jiao Tong University, Shanghai, China, in 2011, and the M.S. degree from the University of Maryland, College Park, MD, USA, in 2015, both in mechanical engineering. He is currently working toward the Ph.D. degree in mechanical engineering with the Department of Mechanical and Aerospace Engineering, North Carolina State University, Raleigh, NC, USA, under the supervision of Dr. Hao Su.

His current research interest includes controller design and implementation of the exoskeleton system.



**Antonio Di Lallo** received the B.S., M.S., and Ph.D. degrees in mechanical engineering from the University of Pisa, Pisa, Italy, in 2012, 2015, and 2019, respectively.

He is currently a Postdoctoral Fellow with the Department of Mechanical and Aerospace Engineering, North Carolina State University, Raleigh, NC, USA. His research interests include soft robots and wearable robots.



**Chunhai Jiao** received the B.S. degree from Northwest A&F University, Xi'an, China in 2004, and the M.S. degree from the City College of New York, New York, USA, in 2020, both in mechanical engineering.

He has been committed to the mechanical design for 18 years in the field of the machine tool, planetary gear transmission, and automation equipment. His current research interests include mechanical design of the lower-limb and upper-limb exoskeleton and other experimental devices to support biomechanical robotic projects.



**Thomas C. Bulea** (Member, IEEE) received the B.S. degree in mechanical engineering from The Ohio State University in 2005, and M.S. and Ph.D. degrees in biomedical engineering from Case Western Reserve University, Cleveland, OH, USA, in 2008 and 2012, respectively.

He completed postdoctoral fellowships from the University of Houston, Houston, TX, USA, and the National Institutes of Health Clinical Center. In 2014, he joined the NIH Clinical Center as a Staff Scientist and is currently a tenure track investigator in the

Neurorehabilitation and Biomechanics Research Section of the Rehabilitation Medicine Department. His research interests include functional neuroimaging, neural interfacing and rehabilitation robotics for evaluation and treatment of movement disorders.

Dr. Bulea was the recipient of the NIH Clinical Center Director's Award and an NIH Director's Award.



Minghui Zheng (Member, IEEE) received the B.E. degree in engineering mechanics and the M.E. degree in control science and engineering from Beihang University, Beijing, China, in 2008 and 2011, respectively, and the Ph.D. degree in mechanical engineering, in 2017, from University of California, Berkeley, CA. USA.

In 2017, she joined University at Buffalo, Buffalo, NY, USA, where she is currently an assistant Professor in mechanical and aerospace engineering. Her research interests include learning, planning, and

control for multiple robotic systems, such as collaborative manipulators for remanufacturing and drones for disaster resilience.

Dr. Zheng was the recipient of the NSF CAREER Award in 2021.



Hao Su (Member, IEEE) received the B.S. degree in automation from the Harbin Institute of Technology, Harbin, China, in 2006, the M.S. degree in mechanical engineering from the State University of New York University at Buffalo, Buffalo, NY, USA, in 2008, and the Ph.D. degree in mechanical engineering from Worcester Polytechnic Institute, Worcester, MA, USA, in 2013.

He is currently an Associate Professor with the Department of Mechanical and Aerospace Engineering, North Carolina State University, Raleigh, NC, USA.

He was the Irwin Zahn Endowed Assistant Professor with the City University of New York, New York, NY, USA, a Research Scientist with Philips Research North America, Cambridge, MA, USA, and a Postdoctoral Fellow with Harvard University, Cambridge, MA, USA, and the Wyss Institute for Biologically Inspired Engineering, Boston, MA, USA. He holds patents on surgical robotics and socially assistive robots.

Prof. Su was the recipient of the National Science Foundation CAREER Award, National Institutes of Health (NIH) R01 Award, Best Student Paper Award of ASME Dynamic Systems Control Division Mechatronics Technical Committee, Toyota Mobility Challenge Discover Award, Best Medical Robotics Paper Runner-up Award in the IEEE International Conference on Robotics and Automation (ICRA), Philips Innovation Transfer Award, the Advanced Simulation and Training Award from the Link Foundation, and Dr. Richard Schlesinger Award from the American Society for Quality. He is currently an Associate Editor for the IEEE ROBOTICS AND AUTOMATION LETTERS, ASME Journal of Mechanisms and Robotics, IEEE International Conference on Robotics and Automation (ICRA), and IEEE/RSJ International Conference on Intelligent Robots and Systems (IROS).